Journal of Computational Physics **156,** 89–136 (1999)
Article ID jcph.1999.6354, available online at http://www.idealibrary.com on IDEAL®

The Space-Time Conservation Element and Solution Element Method: A New High-Resolution and Genuinely Multidimensional Paradigm for Solving Conservation Laws

Sin-Chung Chang,*[,1] Xiao-Yen Wang,† and Chuen-Yen Chow‡

*NASA Glenn Research Center, Cleveland, Ohio 44135; †Taitech Inc. and NASA Glenn Research Center, Cleveland, Ohio 44135; and ‡Department of Aerospace Engineering Sciences, University of Colorado at Boulder, Boulder, Colorado 80309-0429

E-mail: sin-chung.chang@grc.nasa.gov, wangxy@turbot.grc.nasa.gov, and chow@rastro.colorado.edu

Received January 11, 1999; revised August 3, 1999

THIS PAPER IS DEDICATED TO DR. ALLEN I. JANIS, THE FIRST AUTHOR'S PH.D. THESIS ADVISOR AND PROFESSOR EMERITUS AT THE DEPARTMENT OF PHYSICS AND ASTRONOMY, UNIVERSITY OF PITTSBURGH

A new high-resolution and genuinely multidimensional numerical method for solving conservation laws is being developed. It was designed to avoid the limitations of the traditional methods and was built from ground zero with extensive physics considerations. Nevertheless, its foundation is mathematically simple enough that one can build from it a coherent, robust, efficient, and accurate numerical framework. Two basic beliefs that set the new method apart from the established methods are at the core of its development. The first belief is that, in order to capture physics more efficiently and realistically, the modeling focus should be placed on the original integral form of the physical conservation laws, rather than the differential form. The latter form follows from the integral form under the additional assumption that the physical solution is smooth, an assumption that is difficult to realize numerically in a region of rapid change, such as a boundary layer or a shock. The second belief is that, with proper modeling of the integral and differential forms themselves, the resulting numerical solution should automatically be consistent with the properties derived from the integral and differential forms, e.g., the jump conditions across a shock and the properties of characteristics. Therefore a much simpler and more robust method can be developed by avoiding the explicit use of the above derived properties. Specifically, to capture physics as fully as possible, the method requires that: (i) space and time be unified and treated as a single entity; (ii) both local and

[1] Web site: http://www.grc.nasa.gov/www/microbus.

global flux conservation in space and time be enforced; and (iii) a multidimensional scheme be constructed without using the dimensional-splitting approach, such that multidimensional effects and source terms (which are scalars) can be modeled more realistically. To simplify mathematics and broaden its applicability as much as possible, the method attempts to use the simplest logical structures and approximation techniques. Specifically, (i) it uses a staggered space-time mesh such that flux at any interface separating two conservation elements can be evaluated internally in a simpler and more consistent manner, without using a separate flux model; (ii) it avoids the use of many well-established techniques such as Riemann solvers, flux splittings, and monotonicity constraints such that the complications and possibly even the limitations associated with them may be avoided; and (iii) it avoids the use of special techniques that are not applicable to more general problems. Furthermore, triangles in 2D space and tetrahedrons in 3D space are used as the basic building blocks of the spatial meshes, such that the method (i) can be used to construct 2D and 3D nondissipative schemes in a natural manner; and (ii) is compatible with the simplest unstructured meshes. Note that while numerical dissipation is required for shock capturing, it may also result in annihilation of small disturbances such as sound waves and, in the case of flow with a large Reynolds number, may overwhelm physical dissipation. To overcome this difficulty, two different and mutually complementary types of adjustable numerical dissipation are introduced in the present development.

Key Words: space-time; flux conservation; conservation element; solution element; shocks; contact discontinuities.

1. INTRODUCTION

Since its inception in 1991 [1], the space-time conservation element and solution element method (the CE/SE method) [1–25] has been used to obtain highly accurate numerical solutions for 1D, 2D, and 3D flow problems involving shocks, contact discontinuities, vortices, acoustic waves, boundary layers, chemical reactions and hydraulic jump. The method can be applied to both steady and unsteady flow fields in different speed ranges (subsonic, transonic, and supersonic). It is also genuinely multidimensional and compatible with unstructured meshes in both 2D and 3D [12–14]. To answer frequently-asked questions and clarify possible misconceptions, we shall begin this paper with an overall view of the CE/SE method.

Before proceeding, note that in the present paper the reader will often be referred to [7] for the details that are not presented here. This practice is required by the need to cut down the length of this manuscript. To lessen the inconvenience, the paper [7] is posted on and can be downloaded from Section Technical Details of the CE/SE web site: http://www.grc.nasa.gov/www/microbus. Furthermore, the reader can also obtain the hard copies of [7] and other CE/SE related papers by sending e-mail to the first author.

Currently, the field of computational fluid dynamics (CFD) represents a diverse collection of numerical methods, with each of them having its own limitations. Generally speaking, these methods were originally introduced to solve special classes of flow problems. Development of the CE/SE method is motivated by a desire to build a brand new, more general and coherent numerical framework that avoids the limitations of the traditional methods.

The CE/SE method was first published in this journal in 1995 [2]. It was shown in [2] that a simple CE/SE scheme is highly accurate in solving Sod's shock-tube problem. Recently,

the accuracy of this scheme in solving Harten's shock-tube problem was also evaluated against other schemes by Batten *et al.* [3]. They concluded that "the result ... is quite remarkable, considering that the internal details of the Riemann fan are never used and, indeed, are never needed, because the entire Riemann fan is contained within the region of integration." They went on to conclude that "in fact, solutions produced with this scheme are broadly comparable to conventional MUSCL schemes ...." This conclusion is echoed by the results of a recent accuracy study of a CE/SE solver for the Saint Venant equations [4, 5].

The new method is built on a set of design principles that were discussed and justified in [2]. They include: (i) enforcing both local and global flux conservation in space and time, with flux evaluation at an interface being an integral part of the solution procedure and requiring no interpolation or extrapolation; (ii) unifying space and time and treating them as a single entity; (iii) considering mesh values of dependent variables and their derivatives as independent variables, to be solved for simultaneously; (iv) using only local discrete variables rather than global variables like the expansion coefficients used in spectral methods; (v) defining conservation elements and solution elements such that the simplest stencil will result; (vi) requiring that, as much as possible, a numerical analogue be constructed so as to share with the corresponding physical equations the same space–time invariant properties, such that numerical dissipation can be minimized [9]; (vii) excluding the use of characteristics-based techniques (such as Riemann solvers); and (viii) avoiding the use of ad hoc techniques as much as possible.

Moreover, the development of the CE/SE method is also guided by two basic beliefs that set it apart from the established methods. The first belief is that, in order to capture physics more efficiently and realistically, the modeling focus should be placed on the original integral form of the physical conservation laws, rather than the differential form. The latter form follows from the integral form under the additional assumption that the physical solution is smooth, an assumption that is difficult to realize numerically in a region of rapid change, such as a boundary layer or a shock. The second belief is that, with proper modeling of the integral and differential forms themselves, the resulting numerical solution should automatically be consistent with the properties derived from the integral and differential forms, e.g., the jump conditions across a shock and the properties of characteristics. In other words, a much simpler and more robust method can be developed by avoiding the explicit use of the above derived properties.

It will be shown in Section 2 that the spatial meshes used in the new 2D CE/SE schemes to be described are built from triangles (in such a manner that the resulting meshes are completely different from those used in the finite element method). As a result, these schemes are (i) compatible with the simplest unstructured meshes [13] and (ii) constructed without using the traditional dimensional-splitting approach. Note that the dimensional-splitting approach is flawed in several respects [26]. In particular, because a source term is not aligned with a special direction, it is difficult to imagine how this dimensional-splitting approach, in a logically consistent manner, can be used to solve a multidimensional problem involving source terms, such as those modeling chemical energy release [15–17].

Moreover, because the CE/SE 2D schemes share with their 1D versions the same design principles, not only is the extension to 2D a straightforward matter, each of the new 2D schemes also shares with its 1D version virtually identical fundamental characteristics.

At this juncture, note that monotonicity conditions are not observed by general flow fields, e.g., those involving ZND detonation waves [15,16]. For this reason and the fact that their use may introduce excessive numerical dissipation, techniques involving monotonicity constraints so far have not been used in the CE/SE development.

To give the reader, in advance, a concrete example that demonstrates the validity of the two basic beliefs referred to earlier, an extended Sod's shock tube problem is considered here. This extended problem is the original Sod's problem [27] with the additional complication of imposing a nonreflecting boundary condition at each end of the computational domain. Note that the flow under consideration contains discontinuities and, relative to the computational frame, is subsonic throughout. It is well known that implementing a nonreflecting boundary condition for a subsonic flow is much more difficult than doing the same for a supersonic flow. This difficulty is further exacerbated by the fact that the traditional nonreflecting boundary conditions [28], such as those using the properties of characteristics, are all based on an assumption that is not valid for the present case, i.e., that the flow is continuous. In spite of the fact that the extended problem is substantially more difficult than the original problem, the former can be solved by a simple CE/SE scheme that is explained in Section 2.8 of [7]. The main loop of the Fortran program (listed in Appendix A of [7], and also on pp. 229–230 of [6]) implementing this scheme contains only 39 Fortran statements, with none of them calling any subprogram or using any function defined outside the loop. Not only is it very small in size, but this program has a very simple logical structure. With the exception of a single "if" statement used to identify the time levels at which the nonreflecting boundary conditions must be imposed, it contains no conditional Fortran statements or functions such as "if," "amax," or "amin" that are often used in programs implementing high-resolution upwind methods. The small size of the program reflects the simplicity of the techniques employed by the CE/SE method to capture shock waves. It also results from the fact that the nonreflecting boundary conditions used in the present solver are the simple extrapolation conditions: (i)

$$(u_m)_j^n = (u_m)_{j-1/2}^{n-1/2} \quad \text{and} \quad (u_{mx})_j^n = (u_{mx})_{j-1/2}^{n-1/2}, \quad m = 1, 2, 3;\ n = 1, 2, 3, \ldots, \quad (1.1)$$

if (j, n) is a mesh point on the right spatial boundary (see Fig. 1); and (ii)

$$(u_m)_j^n = (u_m)_{j+1/2}^{n-1/2} \quad \text{and} \quad (u_{mx})_j^n = (u_{mx})_{j+1/2}^{n-1/2}, \quad m = 1, 2, 3;\ n = 1, 2, 3, \ldots, \quad (1.2)$$

if (j, n) is a mesh point (a dot in Fig. 1) on the left spatial boundary (note: $(u_m)_j^n$ and $(u_{mx})_j^n$ are the independent numerical variables at the mesh point (j, n) [2]). On the other

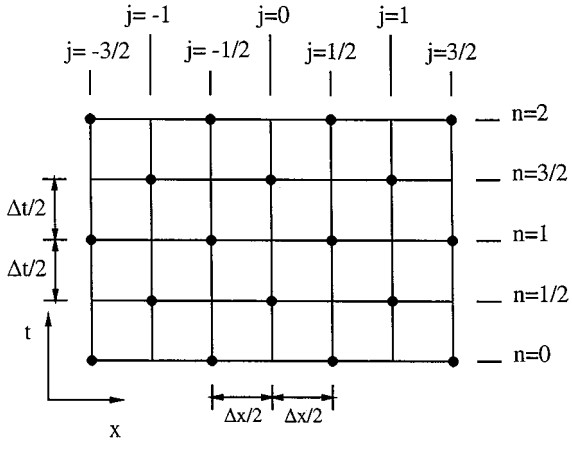

FIG. 1. The staggered space-time mesh.

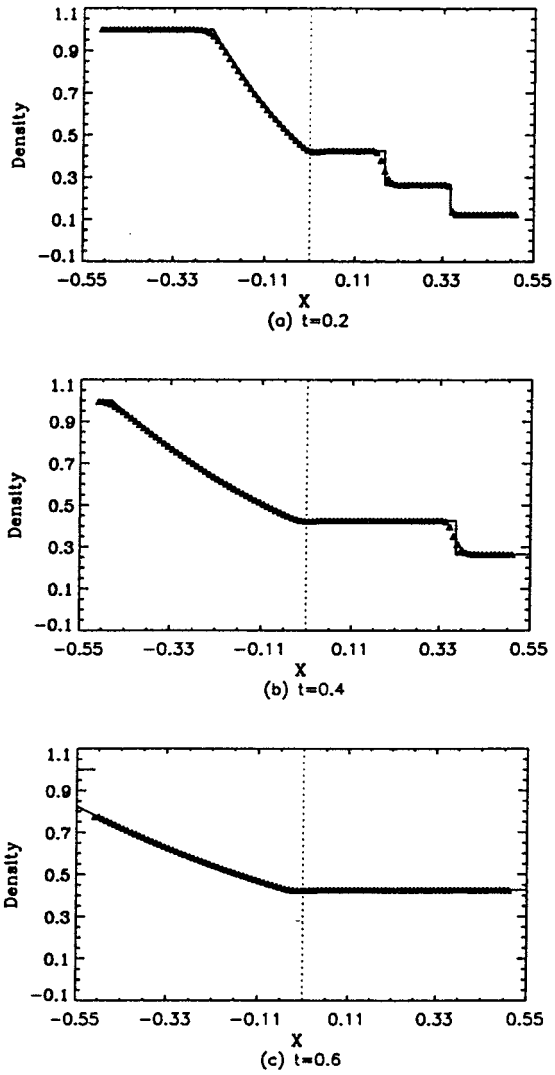

FIG. 2. The CE/SE solution of the extended Sod's problem with boundary conditions Eqs. (1.1) and (1.2) ($\Delta t = 0.004$, $\Delta x = 0.01$, CFL ≈ 0.88).

hand, the absence of Fortran conditional statements is a result of avoiding the use of ad hoc techniques. In spite of its simplicity, according to the comparisons of the numerical results (including the right and left boundary values and denoted by triangles) and the exact solutions (denoted by solid lines) shown in Figs. 2(a–c) (see [7] for velocity and pressure profiles), the present solver is capable of generating nearly perfect nonreflecting solutions. Note that, at $t = 10$, the exact solution is constant across the computational domain. It is shown in [7] that the maximum numerical errors in density, velocity, and pressure are all less than 0.15% of the exact values.

Note that Eqs. (1.1) and (1.2) represent only one of many sets of simple and robust nonreflecting boundary conditions developed in [19] for the CE/SE method. Behind this development is a new concept based entirely on an assumption about the space-time flux distribution in the neighborhood of a spatial boundary. As it turns out, the new concept leads to the surprising conclusion that, albeit of lower order of accuracy, the steady-state

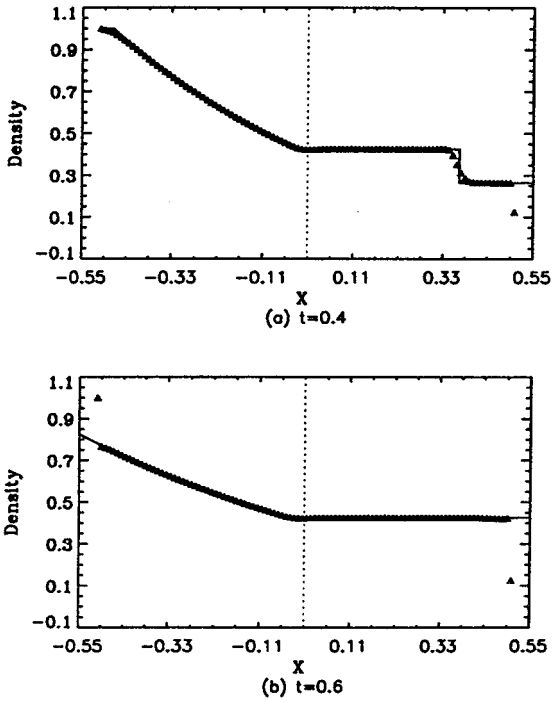

FIG. 3. The CE/SE solution of the extended Sod's problem with boundary conditions Eq. (1.3) ($\Delta t = 0.004$, $\Delta x = 0.01$, CFL ≈ 0.88).

boundary conditions

$$(u_m)_j^n = (u_m)_j^0 \quad \text{and} \quad (u_{mx})_j^n = (u_{mx})_j^0, \quad m = 1, 2, 3;\ n = 1, 2, 3, \ldots, \qquad (1.3)$$

where (j, n) is any mesh point on the right or left boundary, are also nonreflective if they are applied in conjunction with the CE/SE method. The density profiles at $t = 0.4$ and 0.6, computed using an alternative solver that is identical to the solver referred to earlier except that the boundary conditions Eqs. (1.1) and (1.2) are replaced by Eq. (1.3), are compared with the exact solutions in Fig. 3a and 3b (see [7] for the velocity and pressure profiles). Note that, at $t = 0.2$, the numerical solutions generated by the alternative and the original solvers are identical. According to Fig. 3a, by the time $t = 0.4$, the shock wave has passed cleanly through the right boundary. There is good agreement between the numerical solution and the exact solution everywhere in the interior except for a slight disagreement in the vicinity of the right boundary. Note that the right boundary values, which do not vary with time, are discontinuous with respect to the neighboring interior values. According to Fig. 3b, by the time $t = 0.6$, the contact discontinuity has also passed through the right boundary. Agreement between the numerical solution and the exact solution continue to be good in the interior. However, both left and right boundary values are now discontinuous with respect to the neighboring interior values.

Note that several recent applications [20, 21, 25] of the CE/SE method to 2D aeroacoustics problems reveal that: (i) the trivial nature of implementing CE/SE non-reflecting boundary conditions is manifested even for 2D problems; (ii) accuracy of the numerical results for nonlinear Euler problems is comparable to that of a fourth to sixth order compact difference

scheme, even though nominally the CE/SE solver used is only of second-order accuracy; and (iii) most importantly, the CE/SE method is capable of accurately modeling both small disturbances and strong shocks. The following comments are for items (ii) and (iii):

(a) Assuming the same order of accuracy, generally speaking, the accuracy of a scheme that enforces the space–time flux-conservation property is higher than that of a scheme that does not. A compact scheme generally does not enforce the flux-conservation property of the nonlinear Euler equations. On the contrary, not only is the present scheme flux-conserving, its accuracy in nonlinear calculations is enhanced by its surprisingly small dispersive errors [2, 20, 21, 25]. Moreover, the nominal order of accuracy of a Euler solver is determined assuming a linearized form of the Euler equations and that the solution is smooth. Thus, its significance with respect to a nonlinear and/or nonsmooth solution of the full Euler equations may be questionable. As a matter of fact, it was shown by Casper and Carpenter [29] that, for the unsteady Euler equations, solutions generated by high-order schemes (including ENO schemes) generally are only first-order accurate downstream of a shock.

(b) While numerical dissipation is required for shock resolution, it may also result in annihilation of small disturbances such as sound waves. Thus, a solver that can handle both small disturbances and strong shocks must be able to overcome this difficulty.

To pave the way for the later 2D developments, next we shall briefly discuss the a scheme (i.e., the inviscid version of the a-μ scheme [2]) and its role in the CE/SE development. To proceed, note that: (i) the a-μ scheme is a solver of the PDE

$$\frac{\partial u}{\partial t} + a\frac{\partial u}{\partial x} - \mu\frac{\partial^2 u}{\partial x^2} = 0, \tag{1.4}$$

where a and $\mu \geq 0$ are constants; and (ii) the a scheme is nondissipative (note: to the best knowledge of the authors, the a scheme is the only two-level, explicit, and nondissipative solver of Eq. (1.4) with $\mu = 0$). Because the a-μ scheme reduces to the a scheme when the viscosity $\mu = 0$, it follows from (i) and (ii) that the a-μ scheme has the important property that the numerical dissipation of its solutions approaches zero as the physical dissipation approaches zero. Note that, in principle, the nagging problem of physical dissipation being overwhelmed by numerical dissipation in a nearly inviscid problem can be overcome by using a scheme that possesses the above property. Obviously the development of such a scheme must be preceded by that of a nondissipative scheme such as the a scheme.

The problem of physical dissipation being overwhelmed by numerical dissipation does not exist for a pure convection problem. However, as explained in the earlier discussion about the delicate nature of simulating small disturbances in the presence of shocks, numerical dissipation must still be handled carefully in this case. For this reason, the a-ϵ scheme [2] was built from the a scheme so that the numerical dissipation of its solutions can be controlled by the parameter ϵ. Again the a-ϵ scheme reduces to the a scheme when $\epsilon = 0$.

Note that numerical dissipation traditionally is adjusted by varying the magnitude of added artificial dissipation terms. However, after being stripped of these added artificial dissipation terms, almost every traditional scheme is still not free from inherent numerical dissipation. Hence, numerical dissipation generally cannot be avoided completely using the traditional approach.

Finally, note that a thorough discussion about the key differences between the CE/SE method and other established methods is given in Section 1 of [7].

2. GEOMETRICAL DESCRIPTION OF CONSERVATION ELEMENTS IN TWO SPATIAL DIMENSIONS

In [2, 7], it was established that, for each 1D CE/SE solver, there were $2M$ independent marching variables per mesh point with M being the number of conservation laws to be solved. Because M conservation conditions are imposed over each conservation element (CE), two CEs were introduced at each mesh point such that both the 1D *a* scheme and the 1D Euler *a* scheme [7] can be constructed by solving the $2M$ conservation conditions imposed at each mesh point (j, n), for the $2M$ variables associated with the mesh point.

As will be shown in the following sections, for each 2D CE/SE solver, there are $3M$ independent marching variables per mesh point. As a result, three CEs need to be defined at each mesh point. In this section, only the basic geometric structures of these CEs will be described.

Consider a spatial domain formed by congruent triangles (see Fig. 4). The center of each triangle is marked by either a hollow circle or a solid circle. The distribution of these hollow and solid circles is such that if the center of a triangle is marked by a solid (hollow) circle, then the centers of the three neighboring triangles with which the first triangle shares its three sides are marked by hollow (solid) circles. As an example, point G, the center of the triangle $\triangle BDF$, is marked by a solid circle while points A, C, and E, the centers of the triangles $\triangle FMB$, $\triangle BJD$, and $\triangle DLF$, respectively, are marked by hollow circles. These centers are the spatial projections of the space–time mesh points used in the 2D CE/SE solvers.

To specify the exact locations of the mesh points in space-time, one must also specify their temporal coordinates. In the 2D CE/SE development, again we assume that the mesh points are located at the time levels $n = 0, \pm 1/2, \pm 1, \pm 3/2, \ldots$, with $t = n\Delta t$ at the nth time level. Furthermore, we assume that the spatial projections of the mesh points at a

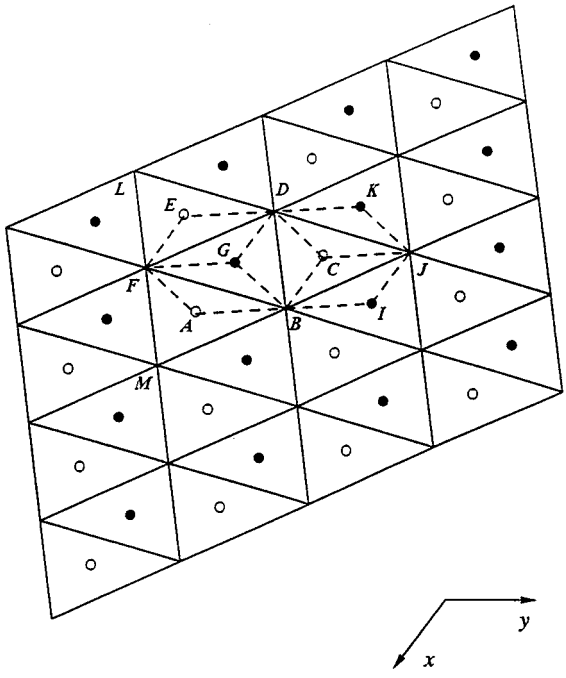

FIG. 4. A spatial domain formed from congruent triangles, showing the spatial projections of the mesh points.

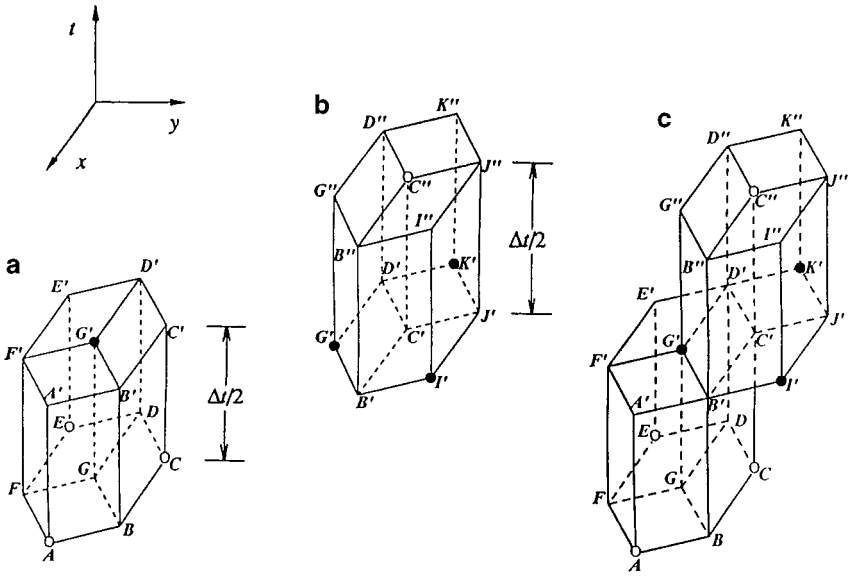

FIG. 5. (a) The CEs associated with G', (b) the CEs associated with C'', and (c) the relative positions of the CEs of successive time steps.

whole-integer (half-integer) time level are the points marked by hollow (solid) circles in Fig. 4.

Let the triangles depicted in Fig. 4 lie on the time level $n = 0$. Then those points marked by hollow circles are the mesh points at this time level. On the other hand, those points marked by solid circles are not the mesh points at the time level $n = 0$. They are the spatial projections of the mesh points at half-integer time levels.

Points A, C, and E, which are depicted in Figs. 4 and 5a, are three mesh points at the time level $n = 0$. Point G', which is depicted in Fig. 5a, is a mesh point at the time level $n = 1/2$. Its spatial projection at the time level $n = 0$ is point G. Because point G is not a mesh point, it is not marked by a circle in the space-time plots given in Figs. 5a and 5c. Hereafter, only a mesh point, e.g., point G', will be marked by a solid or hollow circle in a space–time plot.

The CEs associated with a mesh point at a half-integer time level, such as point G', are defined to be the space–time quadrilateral cylinders $GFABG'F'A'B'$, $GBCDG'B'C'D'$, and $GDEFG'D'E'F'$. Similarly, the CEs associated with a mesh point at a whole-integer time-level, such as point C'', are the quadrilateral cylinders $C'J'K'D'C''J''K''D''$, $C'D'G'B'C''D''G''B''$, and $C'B'I'J'C''B''I''J''$ (see Fig. 5b). The relative space-time positions of the six CEs associated with mesh points G' and C'' are depicted in Fig. 5c.

Note that (i) points A, C, E, and G are the geometric centers of four neighboring congruent triangles $\triangle FMB$, $\triangle BJD$, $\triangle DLF$, and $\triangle BDF$, respectively; and (ii) among those depicted in Fig. 4, any pair of triangles sharing a common side forms a parallelogram. As a result, one concludes that

(a) $\overline{CD}$, $\overline{GE}$, $\overline{BG}$, and $\overline{AF}$ are parallel line segments of equal length.
(b) $\overline{AB}$, $\overline{GC}$, $\overline{FG}$, and $\overline{ED}$ are parallel line segments of equal length.
(c) $\overline{BC}$, $\overline{GD}$, $\overline{AG}$, and $\overline{FE}$ are parallel line segments of equal length.
(d) Point G is the geometric center of the hexagon $ABCDEF$ and the triangle ACE.

Finally note that, because the hexagon $BIJKDG$ (depicted in Fig. 4) is congruent to the hexagon $ABCDEF$, a set of geometric relations similar to those listed above also exists for the vertices and the center of the hexagon $BIJKDG$.

3. THE 2D *a* SCHEME

In this section, we consider a dimensionless form of the 2D convection equation, i.e.,

$$\frac{\partial u}{\partial t} + a_x \frac{\partial u}{\partial x} + a_y \frac{\partial u}{\partial y} = 0, \tag{3.1}$$

where a_x and a_y are constants. Let $x_1 = x$, $x_2 = y$, and $x_3 = t$ be the coordinates of a three-dimensional Euclidean space E_3. By using Gauss' divergence theorem in the space-time E_3, it can be shown that Eq. (3.1) is the differential form of the integral conservation law

$$\oint_{S(V)} \mathbf{h} \cdot d\mathbf{s} = 0. \tag{3.2}$$

Here, (i) $S(V)$ is the boundary of an arbitrary space-time region V in E_3, (ii)

$$\mathbf{h} \stackrel{\text{def}}{=} (a_x u, a_y u, u) \tag{3.3}$$

is a current density vector in E_3, and (iii) $d\mathbf{s} = d\sigma\, \mathbf{n}$ with $d\sigma$ and $\mathbf{n}$, respectively, being the area and the outward unit normal of a surface element on $S(V)$. Note that (i) $\mathbf{h} \cdot d\mathbf{s}$ is the space-time flux of $\mathbf{h}$ leaving the region V through the surface element $d\mathbf{s}$, and (ii) all mathematical operations can be carried out as though E_3 were an ordinary three-dimensional Euclidean space.

In the following analysis, the nontraditional space-time mesh that was sketched in Section 2 will be rigorously defined. To proceed, the spatial projections of the mesh points depicted in Fig. 4 are reproduced in Fig. 6. Note that the dashed lines that appear in Fig. 6 are the spatial projections of the vertical interfaces (see Figs. 5a–c) that separate different CEs. Also note that, as a result of the geometric relations listed at the end of Section 2, any

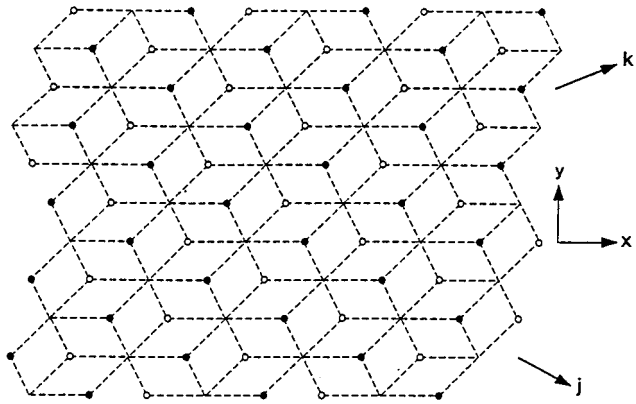

FIG. 6. The relative spatial positions of the mesh points $\in \Omega_1$ and the mesh points $\in \Omega_2$ (dashed lines are spatial boundaries of the conservation elements depicted in Figs. 9a and 10a).

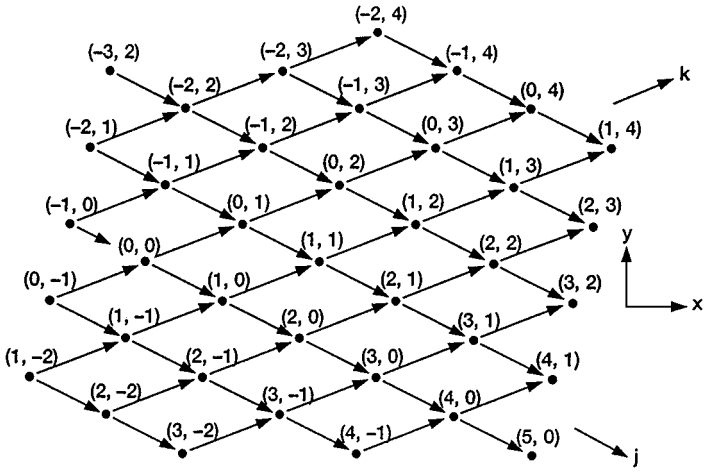

FIG. 7. The spatial mesh indices (j, k) of the mesh points $\in \Omega_1 (n = \pm 1/2, \pm 3/2, \pm 5/2, \cdots)$.

dashed line can point only in one of three different fixed directions. We assume that the congruent triangles depicted in Fig. 4 are aligned such that one of the above fixed directions is the x-direction.

Each mesh point marked by a solid or hollow circle is assigned a pair of spatial indices (j, k) according to the location of its spatial projection. Obviously, a mesh point can be uniquely identified by its spatial indices (j, k) and the time level n where it resides. According to Figs. 7 and 8, the spatial projections of the mesh points that share the same value of j (k) lie on a straight line on the x–y plane with this straight line pointing in the direction of the k- $(j$-$)$ mesh axis.

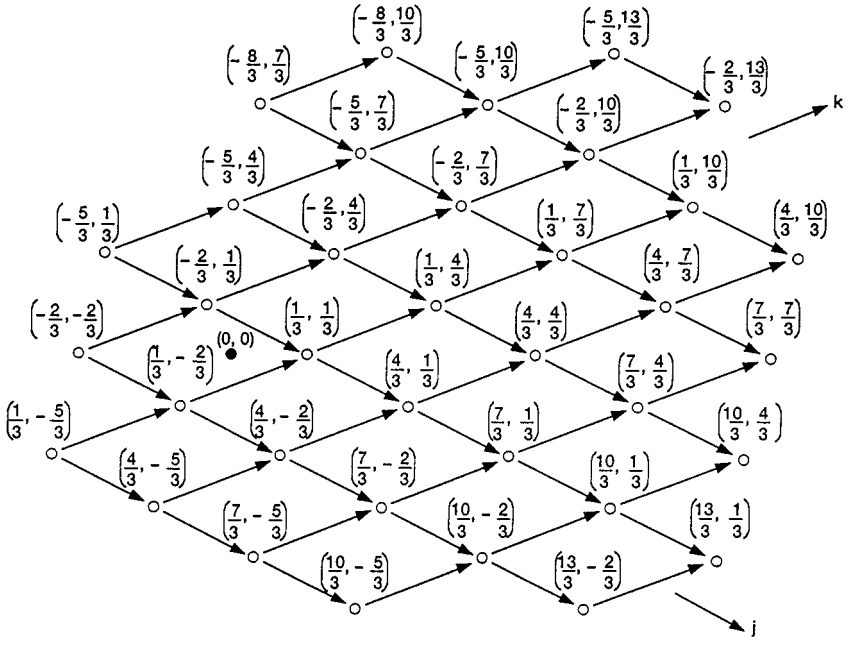

FIG. 8. The spatial mesh indices (j, k) of the mesh points $\in \Omega_2 (n = 0, \pm 1, \pm 2, \cdots)$.

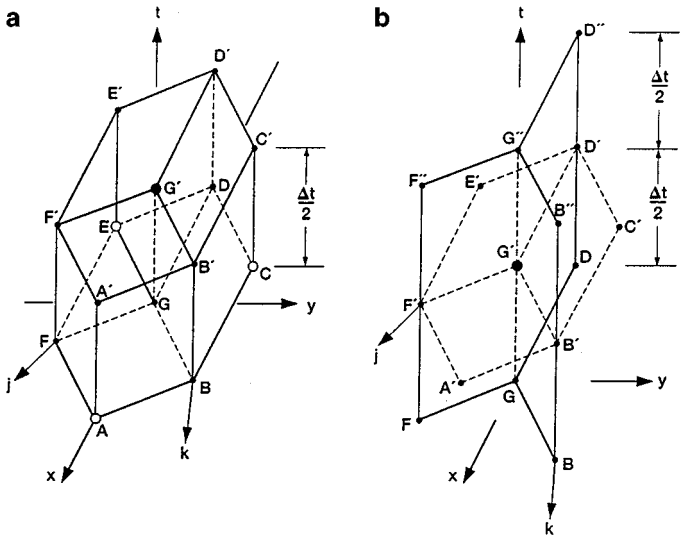

FIG. 9. (a) Conservation elements $CE_r(j, k, n), r = 1, 2, 3$, for any $(j, k, n) \in \Omega_1$. (b) Solution element $SE(j, k, n)$ for any $(j, k, n) \in \Omega_1$.

Let

$$t^n \stackrel{\text{def}}{=} n\Delta t, \quad n = 0, \pm 1/2, \pm 1, \pm 3/2, \ldots. \tag{3.4}$$

Let j and k be spatial mesh indices with $j, k = 0, \pm 1/3, \pm 2/3, \pm 1, \ldots$. Let Ω_1 denote the set of mesh points (j, k, n) with $j, k = 0, \pm 1, \pm 2, \ldots$, and $n = \pm 1/2, \pm 3/2, \pm 5/2, \ldots$. These mesh points are marked by solid circles. Let Ω_2 denote the set of mesh points (j, k, n) with $j, k = 1/3, 1/3 \pm 1, 1/3 \pm 2, \ldots$, and $n = 0, \pm 1, \pm 2, \ldots$. These mesh points are marked by hollow circles. The union of Ω_1 and Ω_2 will be denoted by Ω.

Each mesh point $(j, k, n) \in \Omega$ is associated with (i) three conservation elements, denoted by $\text{CE}_r(j, k, n)$, $r = 1, 2, 3$ (see Figs. 9a and 10a); and (ii) a solution element, denoted by $\text{SE}(j, k, n)$ (see Figs. 9b and 10b). Note that (i) E_3 can be filled with the CEs defined above; (ii) the boundary of a CE is formed by the subsets of two neighboring SEs; and (iii) the CEs and the SE associated with a mesh point $(j, k, n) \in \Omega_1$ differ from those associated with a mesh point $(j, k, n) \in \Omega_2$ in their space-time orientations.

By using the geometric relations listed at the end of Section 2, one can conclude that the spatial coordinates of the vertices of the hexagon $ABCDEF$, which appears in both Figs. 9a and 10a, are uniquely determined by three positive parameters w, b, and h (see Fig. 11a) if (i) one assumes that $\overline{DA}$ is aligned with the x-direction and (ii) the spatial coordinates of point G (the centroid of the hexagon) are given. Note that w, b, and h, respectively, are the lengths of the line segments $\overline{DM}$, $\overline{MH}$, and $\overline{BH}$ with (i) $\overline{DM}$ being a median of the

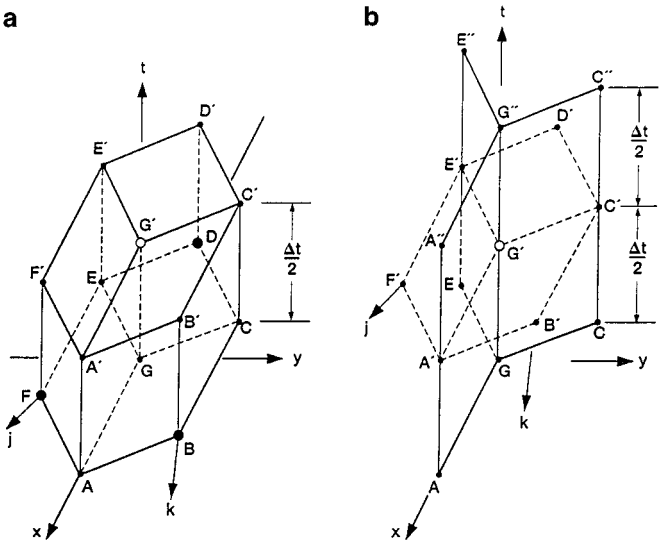

FIG. 10. (a) Conservation elements $CE_r(j,k,n), r=1,2,3$, for any $(j,k,n)\in\Omega_2$. (b) Solution element SE (j,k,n) for any $(j,k,n)\in\Omega_2$.

triangle $\triangle BDF$ and (ii) points G, M, and H being on the line segment $\overline{DA}$. Also note that a dashed line in Fig. 6 may appear in other figures as a solid line.

Let the space-time mesh be uniform, i.e., the parameters Δt, w, b, and h are constants. Let $x_{j,k}$ and $y_{j,k}$ be the x- and y-coordinates of any mesh points $(j,k,n)\in\Omega$. Let $x_{0,0}=0$ and $y_{0,0}=0$. Then information provided by Figs. 11a and 11b implies that

$$x_{j,k}=(j+k)w+(k-j)b,\quad y_{j,k}=(k-j)h. \tag{3.5}$$

For any $(x,y,t)\in \mathrm{SE}(j,k,n)$, $u(x,y,t)$ and $\mathbf{h}(x,y,t)$, respectively, are approximated by

$$u^*(x,y,t;\,j,k,n)\stackrel{\text{def}}{=}u^n_{j,k}+(u_x)^n_{j,k}(x-x_{j,k})+(u_y)^n_{j,k}(y-y_{j,k})+(u_t)^n_{j,k}(t-t^n) \tag{3.6}$$

and

$$\mathbf{h}^*(x,y,t;\,j,k,n)\stackrel{\text{def}}{=}[a_x u^*(x,y,t;\,j,k,n),\,a_y u^*(x,y,t;\,j,k,n),\,u^*(x,y,t;\,j,k,n)], \tag{3.7}$$

where $u^n_{j,k}$, $(u_x)^n_{j,k}$, $(u_y)^n_{j,k}$, and $(u_t)^n_{j,k}$ are constants within $\mathrm{SE}(j,k,n)$. Note that Eq. (3.7) is the numerical analogue of Eq. (3.3).

$u=u^*(x,y,t;\,j,k,n)$ is required to satisfy Eq. (3.1) within $\mathrm{SE}(j,k,n)$. Thus,

$$(u_t)^n_{j,k}=-\left[a_x(u_x)^n_{j,k}+a_y(u_y)^n_{j,k}\right]. \tag{3.8}$$

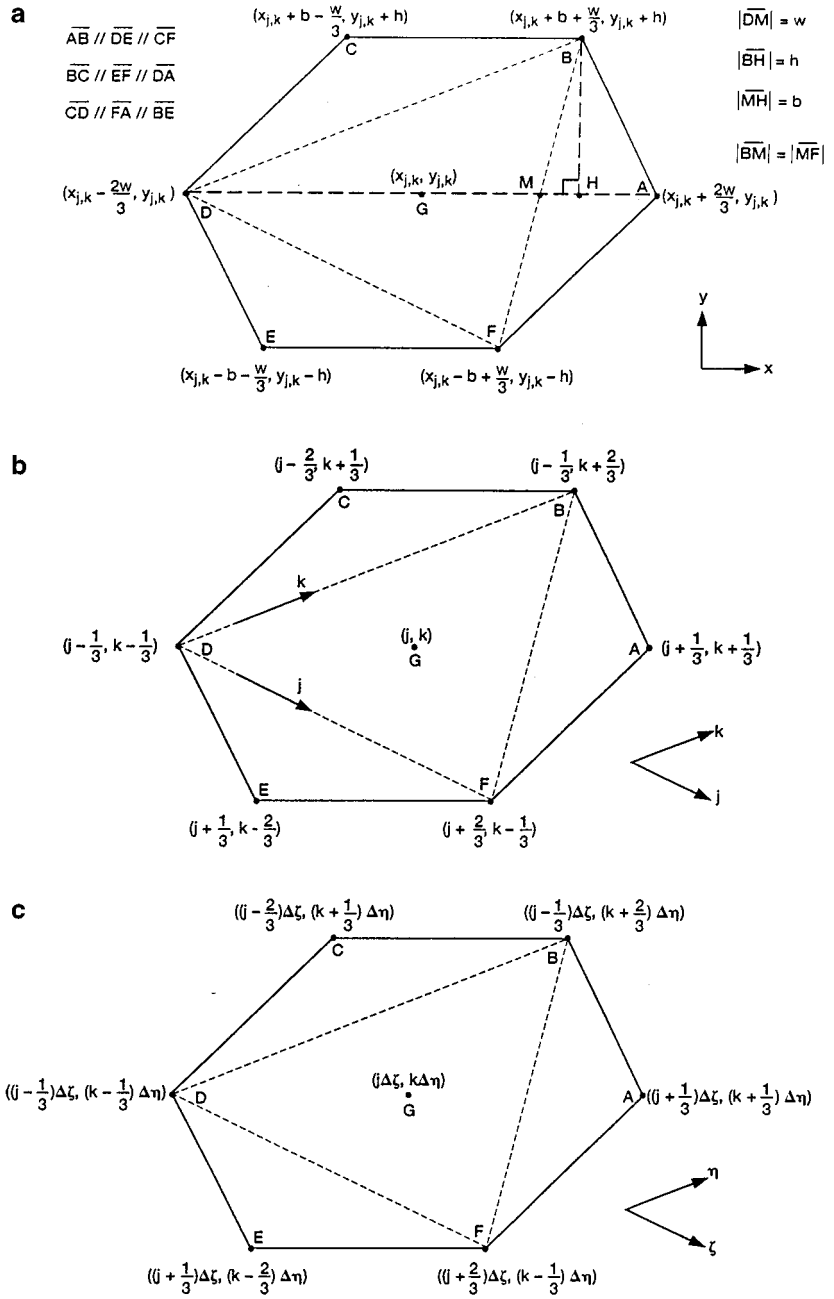

FIG. 11. Geometry of the hexagon $ABCDEF$. (a) Relative positions of the vertices in terms of (x, y). (b) Relative positions of the vertices in terms of (j, k). (c) Relative positions of the vertices in terms of (ζ, η).

Equations (3.6) and (3.8) imply that

$$u^*(x, y, t; j, k, n) = u^n_{j,k} + (u_x)^n_{j,k}\left[(x - x_{j,k}) - a_x(t - t^n)\right] + (u_y)^n_{j,k}\left[(y - y_{j,k}) - a_y(t - t^n)\right]. \tag{3.9}$$

Thus, there are three independent marching variables, i.e., $u^n_{j,k}$, $(u_x)^n_{j,k}$, and $(u_y)^n_{j,k}$ associated with a mesh point $(j, k, n) \in \Omega$. For any $(j, k, n) \in \Omega_1$, these variables will be

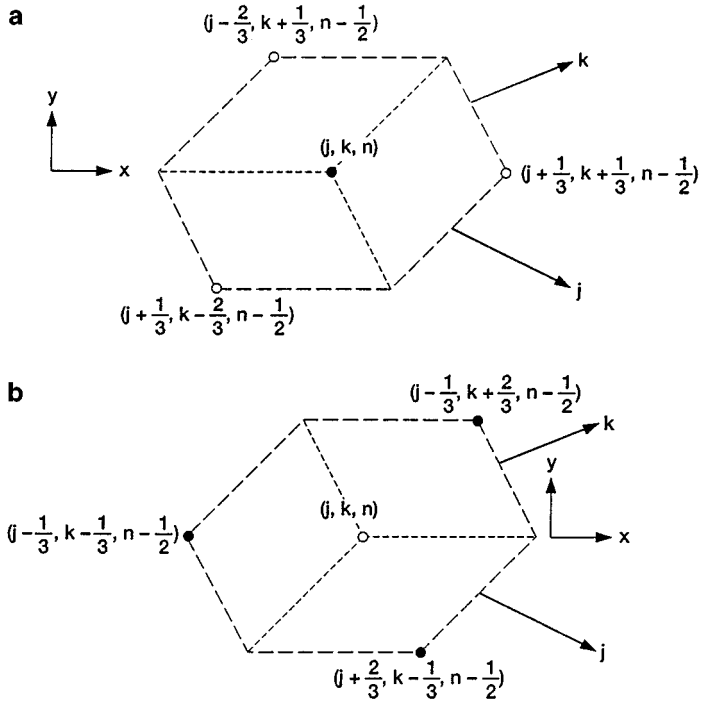

FIG. 12. (a) The mesh points (j, k, n), $(j+1/3, k+1/3, n-1/2)$, $(j-2/3, k+1/3, n-1/2)$ and $(j+1/3, k-2/3, n-1/2)$ that belong to Ω_1. (b) The mesh points (j, k, n), $(j-1/3, k-1/3, n-1/2)$, $(j+2/3, k-1/3, n-1/2)$, and $(j-1/3, k+2/3, n-1/2)$ that belong to Ω_2.

determined in terms of those associated with the mesh points $(j+1/3, k+1/3, n-1/2)$, $(j-2/3, k+1/3, n-1/2)$, and $(j+1/3, k-2/3, n-1/2)$ (see Fig. 12a) by using the three flux conservation relations

$$\oint_{S(CE_r(j,k,n))} \mathbf{h}^* \cdot d\mathbf{s} = 0, \quad r = 1, 2, 3. \tag{3.10}$$

Similarly, the marching variables at any $(j, k, n) \in \Omega_2$ are determined in terms of those associated with the mesh points $(j-1/3, k-1/3, n-1/2)$, $(j+2/3, k-1/3, n-1/2)$, and $(j-1/3, k+2/3, n-1/2)$ (see Fig. 12b) by using the three flux conservation relations Eq. (3.10). Obviously, Eq. (3.10) is the numerical analogue of Eq. (3.2).

As a result of Eq. (3.10), the total flux leaving the boundary of any CE is zero. Because the flux at any interface separating two neighboring CEs is calculated using the information from a single SE, the flux entering one of these CEs is equal to that leaving another. It follows that the local conservation conditions Eq. (3.10) will lead to a global conservation condition, i.e., the total flux leaving the boundary of any space-time region that is the union of any combination of CEs will also vanish.

In the following, several preliminaries will be given prior to the evaluation of Eq. (3.10). To proceed, note that a mesh line with j and n being constant or a mesh line with k and n being constant is not aligned with the x-axis or the y-axis. We shall introduce a new spatial coordinate system (ζ, η) with its axes aligned with the above mesh lines (see Fig. 11c).

Let $\mathbf{e}_x$ and $\mathbf{e}_y$ be the unit vectors in the x- and the y-directions, respectively. Let $\mathbf{e}_\zeta$ and $\mathbf{e}_\eta$ be the unit vectors in the directions of $\overrightarrow{\mathrm{DF}}$ and $\overrightarrow{\mathrm{DB}}$ (i.e., the j- and the k-directions—see

Figs. 11a–11c), respectively. Let the origin of (x, y) also be that of (ζ, η). Then, at any point in E_3, the coordinates (ζ, η) are defined in terms of (x, y) using the relation

$$\zeta \mathbf{e}_\zeta + \eta \mathbf{e}_\eta = x \mathbf{e}_x + y \mathbf{e}_y. \tag{3.11}$$

Using the above definition, it can be shown that [7]

$$\begin{pmatrix} x \\ y \end{pmatrix} = T \begin{pmatrix} \zeta \\ \eta \end{pmatrix}, \quad \text{and} \quad \begin{pmatrix} \zeta \\ \eta \end{pmatrix} = T^{-1} \begin{pmatrix} x \\ y \end{pmatrix} \tag{3.12}$$

with

$$T \stackrel{\text{def}}{=} \begin{pmatrix} \frac{w-b}{\Delta\zeta} & \frac{w+b}{\Delta\eta} \\ -\frac{h}{\Delta\zeta} & \frac{h}{\Delta\eta} \end{pmatrix}, \quad \text{and} \quad T^{-1} \stackrel{\text{def}}{=} \begin{pmatrix} \frac{\Delta\zeta}{2w} & -\frac{(w+b)\Delta\zeta}{2wh} \\ \frac{\Delta\eta}{2w} & \frac{(w-b)\Delta\eta}{2wh} \end{pmatrix}. \tag{3.13}$$

Here,

$$\Delta\zeta \stackrel{\text{def}}{=} |\overline{DF}| = \sqrt{(w-b)^2 + h^2}, \quad \text{and} \quad \Delta\eta \stackrel{\text{def}}{=} |\overline{DB}| = \sqrt{(w+b)^2 + h^2}. \tag{3.14}$$

With the aid of Eqs. (3.5), (3.12), and (3.13), it can be shown that the coordinates (ζ, η) of any mesh point $(j, k, n) \in \Omega$ are given by

$$\zeta = j\Delta\zeta, \quad \text{and} \quad \eta = k\Delta\eta; \tag{3.15}$$

i.e., $\Delta\zeta$ and $\Delta\eta$ are the mesh intervals in the ζ- and the η-directions, respectively.

Next we shall introduce several coefficients that are tied to the coordinate system (ζ, η). Let

$$\begin{pmatrix} a_\zeta \\ a_\eta \end{pmatrix} \stackrel{\text{def}}{=} T^{-1} \begin{pmatrix} a_x \\ a_y \end{pmatrix}. \tag{3.16}$$

Also, for any $(j, k, n) \in \Omega$, let

$$\begin{pmatrix} (u_\zeta)^n_{j,k} \\ (u_\eta)^n_{j,k} \end{pmatrix} \stackrel{\text{def}}{=} T^t \begin{pmatrix} (u_x)^n_{j,k} \\ (u_y)^n_{j,k} \end{pmatrix}, \tag{3.17}$$

where T^t is the transpose of T. Equations (3.8), (3.9), (3.12), (3.13), (3.16), and (3.17) imply that

$$(u_t)^n_{j,k} = -\big[a_\zeta (u_\zeta)^n_{j,k} + a_\eta (u_\eta)^n_{j,k}\big] \tag{3.18}$$

and

$$u^*(x, y, t;\, j, k, n) = u^\star(\zeta, \eta, t;\, j, k, n), \tag{3.19}$$

where

$$\begin{aligned} u^\star(\zeta, \eta, t;\, j, k, n) \stackrel{\text{def}}{=} u^n_{j,k} &+ (u_\zeta)^n_{j,k}\big[(\zeta - j\Delta\zeta) - a_\zeta (t - t^n)\big] \\ &+ (u_\eta)^n_{j,k}\big[(\eta - k\Delta\eta) - a_\eta (t - t^n)\big]. \end{aligned} \tag{3.20}$$

Next, let (i)

$$\nu_\zeta \stackrel{\text{def}}{=} \frac{3\Delta t}{2\Delta\zeta} a_\zeta, \quad \text{and} \quad \nu_\eta \stackrel{\text{def}}{=} \frac{3\Delta t}{2\Delta\eta} a_\eta \tag{3.21}$$

and (ii)

$$(u_\zeta^+)_{j,k}^n \stackrel{\text{def}}{=} \frac{\Delta\zeta}{6}(u_\zeta)_{j,k}^n, \quad \text{and} \quad (u_\eta^+)_{j,k}^n \stackrel{\text{def}}{=} \frac{\Delta\eta}{6}(u_\eta)_{j,k}^n. \tag{3.22}$$

The coefficients defined in Eqs. (3.21) and (3.22) can be considered as the normalized counterparts of those defined in Eqs. (3.16) and (3.17). Furthermore, because $\Delta\zeta$ and $\Delta\eta$ are the mesh intervals in the ζ- and η-directions, respectively, Eq. (3.21) implies that $(2/3)\nu_\zeta$ and $(2/3)\nu_\eta$, respectively, are equal to the Courant numbers in the ζ- and η-directions, respectively.

Furthermore, to simplify the following development, let

$$(j,k;1,1) \stackrel{\text{def}}{=} j+1/3, k+1/3, \quad (j,k;2,1) \stackrel{\text{def}}{=} j-1/3, k-1/3 \tag{3.23}$$

$$(j,k;1,2) \stackrel{\text{def}}{=} j-2/3, k+1/3, \quad (j,k;2,2) \stackrel{\text{def}}{=} j+2/3, k-1/3 \tag{3.24}$$

$$(j,k;1,3) \stackrel{\text{def}}{=} j+1/3, k-2/3, \quad (j,k;2,3) \stackrel{\text{def}}{=} j-1/3, k+2/3. \tag{3.25}$$

Note that (i) $(j,k;1,r)$, $r=1,2,3$, are the spatial mesh indices of points A, C, and E depicted in Fig. 9a, respectively, and (ii) $(j,k;2,r)$, $r=1,2,3$, are the spatial mesh indices of points D, F, and B depicted in Fig. 10a, respectively.

Equation (3.10) is evaluated in Appendix B of [7]. The evaluation is facilitated by the following observations: (i) the boundary of each CE is formed by six quadrilaterals in E_3 with each quadrilateral belonging to a single SE (see Figs. 9 and 10); and (ii) because $u^*(x,y,t;j,k,n)$ is linear in x, y, and t (see Eqs. (3.9)), Eq. (3.7) implies that, for any $r=1,2,3$, the total flux of $\mathbf{h}^*$ leaving $\text{CE}_r(j,k,n)$ through any one of its six boundary quadrilaterals is equal to the scalar product of the vector $\mathbf{h}^*$ evaluated at the centroid of the quadrilateral and the surface vector (i.e., the unit normal multiplied by the surface area) of the quadrilateral. Let $(j,k,n) \in \Omega_q$ with $q=1,2$. Then, for any $r=1,2,3$, the result of evaluation can be expressed as

$$\left[\sigma_{r1}^{(q)+}u + \sigma_{r2}^{(q)+}u_\zeta^+ + \sigma_{r3}^{(q)+}u_\eta^+\right]_{j,k}^n = \left[\sigma_{r1}^{(q)-}u + \sigma_{r2}^{(q)-}u_\zeta^+ + \sigma_{r3}^{(q)-}u_\eta^+\right]_{(j,k;q,r)}^{n-1/2}, \tag{3.26}$$

where the coefficients $\sigma_{rs}^{(q)\pm}(q=1,2 \text{ and } r,s=1,2,3)$ are defined by

$$\sigma_{11}^{(1)\pm} \stackrel{\text{def}}{=} 1-\nu_\zeta-\nu_\eta, \quad \sigma_{11}^{(2)\pm} \stackrel{\text{def}}{=} 1+\nu_\zeta+\nu_\eta \tag{3.27}$$

$$\sigma_{12}^{(1)\pm} \stackrel{\text{def}}{=} \pm(1-\nu_\zeta-\nu_\eta)(1+\nu_\zeta), \quad \sigma_{12}^{(2)\pm} \stackrel{\text{def}}{=} \mp(1+\nu_\zeta+\nu_\eta)(1-\nu_\zeta) \tag{3.28}$$

$$\sigma_{13}^{(1)\pm} \stackrel{\text{def}}{=} \pm(1-\nu_\zeta-\nu_\eta)(1+\nu_\eta), \quad \sigma_{13}^{(2)\pm} \stackrel{\text{def}}{=} \mp(1+\nu_\zeta+\nu_\eta)(1-\nu_\eta) \tag{3.29}$$

$$\sigma_{21}^{(1)\pm} \stackrel{\text{def}}{=} 1+\nu_\zeta, \quad \sigma_{21}^{(2)\pm} \stackrel{\text{def}}{=} 1-\nu_\zeta \tag{3.30}$$

$$\sigma_{22}^{(1)\pm} \stackrel{\text{def}}{=} \mp(1+\nu_\zeta)(2-\nu_\zeta), \quad \sigma_{22}^{(2)\pm} \stackrel{\text{def}}{=} \pm(1-\nu_\zeta)(2+\nu_\zeta) \tag{3.31}$$

$$\sigma_{23}^{(1)\pm} \stackrel{\text{def}}{=} \pm(1+\nu_\zeta)(1+\nu_\eta), \quad \sigma_{23}^{(2)\pm} \stackrel{\text{def}}{=} \mp(1-\nu_\zeta)(1-\nu_\eta) \tag{3.32}$$

$$\sigma_{31}^{(1)\pm} \stackrel{\text{def}}{=} 1+\nu_\eta, \quad \sigma_{31}^{(2)\pm} \stackrel{\text{def}}{=} 1-\nu_\eta \tag{3.33}$$

$$\sigma_{32}^{(1)\pm} \stackrel{\text{def}}{=} \pm(1+\nu_\eta)(1+\nu_\zeta), \quad \sigma_{32}^{(2)\pm} \stackrel{\text{def}}{=} \mp(1-\nu_\eta)(1-\nu_\zeta) \tag{3.34}$$

and

$$\sigma_{33}^{(1)\pm} \stackrel{\text{def}}{=} \mp(1+\nu_\eta)(2-\nu_\eta), \quad \sigma_{33}^{(2)\pm} \stackrel{\text{def}}{=} \pm(1-\nu_\eta)(2+\nu_\eta). \tag{3.35}$$

Note that, to simplify notation, in Eq. (3.26) and hereafter we adopt a convention that can be explained using the expression on the left side of Eq. (3.26) as an example; i.e.,

$$\left[\sigma_{r1}^{(q)+}u+\sigma_{r2}^{(q)+}u_\xi^+ +\sigma_{r3}^{(q)+}u_\eta^+\right]_{j,k}^n=\sigma_{r1}^{(q)+}u_{j,k}^n+\sigma_{r2}^{(q)+}(u_\xi^+)_{j,k}^n+\sigma_{r3}^{(q)+}(u_\eta^+)_{j,k}^n.$$

Let (i) $1-\nu_\xi-\nu_\eta\neq 0$, (ii) $1+\nu_\xi\neq 0$, (iii) $1+\nu_\eta\neq 0$, (iv) $1+\nu_\xi+\nu_\eta\neq 0$, (v) $1-\nu_\xi\neq 0$, and (vi) $1-\nu_\eta\neq 0$, i.e.,

$$\left[1-(\nu_\xi+\nu_\eta)^2\right]\left(1-\nu_\xi^2\right)\left(1-\nu_\eta^2\right)\neq 0, \tag{3.36}$$

then the six equations ($q=1,2$ and $r=1,2,3$) given in Eq. (3.26) can be simplified as

$$[u+(1+\nu_\xi)u_\xi^+ +(1+\nu_\eta)u_\eta^+]_{j,k}^n=s_1^{(1)},\quad (j,k,n)\in\Omega_1 \tag{3.37}$$

$$[u-(2-\nu_\xi)u_\xi^+ +(1+\nu_\eta)u_\eta^+]_{j,k}^n=s_2^{(1)},\quad (j,k,n)\in\Omega_1 \tag{3.38}$$

$$[u+(1+\nu_\xi)u_\xi^+ -(2-\nu_\eta)u_\eta^+]_{j,k}^n=s_3^{(1)},\quad (j,k,n)\in\Omega_1 \tag{3.39}$$

$$[u-(1-\nu_\xi)u_\xi^+ -(1-\nu_\eta)u_\eta^+]_{j,k}^n=s_1^{(2)},\quad (j,k,n)\in\Omega_2 \tag{3.40}$$

$$[u+(2+\nu_\xi)u_\xi^+ -(1-\nu_\eta)u_\eta^+]_{j,k}^n=s_2^{(2)},\quad (j,k,n)\in\Omega_2 \tag{3.41}$$

and

$$[u-(1-\nu_\xi)u_\xi^+ +(2+\nu_\eta)u_\eta^+]_{j,k}^n=s_3^{(2)},\quad (j,k,n)\in\Omega_2, \tag{3.42}$$

respectively. Here

$$s_1^{(1)}\stackrel{\text{def}}{=}[u-(1+\nu_\xi)u_\xi^+ -(1+\nu_\eta)u_\eta^+]_{(j,k;1,1)}^{n-1/2},\quad (j,k,n)\in\Omega_1 \tag{3.43}$$

$$s_2^{(1)}\stackrel{\text{def}}{=}[u+(2-\nu_\xi)u_\xi^+ -(1+\nu_\eta)u_\eta^+]_{(j,k;1,2)}^{n-1/2},\quad (j,k,n)\in\Omega_1 \tag{3.44}$$

$$s_3^{(1)}\stackrel{\text{def}}{=}[u-(1+\nu_\xi)u_\xi^+ +(2-\nu_\eta)u_\eta^+]_{(j,k;1,3)}^{n-1/2},\quad (j,k,n)\in\Omega_1 \tag{3.45}$$

$$s_1^{(2)}\stackrel{\text{def}}{=}[u+(1-\nu_\xi)u_\xi^+ +(1-\nu_\eta)u_\eta^+]_{(j,k;2,1)}^{n-1/2},\quad (j,k,n)\in\Omega_2 \tag{3.46}$$

$$s_2^{(2)}\stackrel{\text{def}}{=}[u-(2+\nu_\xi)u_\xi^+ +(1-\nu_\eta)u_\eta^+]_{(j,k;2,2)}^{n-1/2},\quad (j,k,n)\in\Omega_2 \tag{3.47}$$

and

$$s_3^{(2)}\stackrel{\text{def}}{=}[u+(1-\nu_\xi)u_\xi^+ -(2+\nu_\eta)u_\eta^+]_{(j,k;2,3)}^{n-1/2},\quad (j,k,n)\in\Omega_2. \tag{3.48}$$

The current 2D *a* scheme will be constructed using Eqs. (3.37)–(3.42) without assuming Eq. (3.36). Note that Eqs. (3.37)–(3.42) imply Eq. (3.26) for any ν_ξ and ν_η. However, the reverse is false unless Eq. (3.36) is assumed.

For either $q=1$ or $q=2$, by summing over the three equations $r=1,2,3$ given in Eq. (3.26) and using the properties

$$\sigma_{11}^{(q)\pm}+\sigma_{21}^{(q)\pm}+\sigma_{31}^{(q)\pm}=3,\quad q=1,2 \tag{3.49}$$

and

$$\sigma_{12}^{(q)\pm}+\sigma_{22}^{(q)\pm}+\sigma_{32}^{(q)\pm}=\sigma_{13}^{(q)\pm}+\sigma_{23}^{(q)\pm}+\sigma_{33}^{(q)\pm}=0,\quad q=1,2 \tag{3.50}$$

one concludes that, for any $(j, k, n) \in \Omega_q$,

$$u^n_{j,k} = \frac{1}{3}\sum_{r=1}^{3}\left[\sigma^{(q)-}_{r1}u + \sigma^{(q)-}_{r2}u^+_\zeta + \sigma^{(q)-}_{r3}u^+_\eta\right]^{n-1/2}_{(j,k;q,r)}, \quad q = 1, 2. \tag{3.51}$$

Also, it follows from Eqs. (3.37)–(3.42) that, for any $(j, k, n) \in \Omega_q$,

$$(u^+_\zeta)^n_{j,k} = \left(u^{a+}_\zeta\right)^n_{j,k} \quad \text{and} \quad \left(u^+_\eta\right)^n_{j,k} = \left(u^{q+}_\eta\right)^n_{j,k}, \tag{3.52}$$

where

$$\left(u^{a+}_\zeta\right)^n_{j,k} \stackrel{\text{def}}{=} \frac{(-1)^q}{3}\left(s^{(q)}_2 - s^{(q)}_1\right) \quad \text{and} \quad \left(u^{a+}_\eta\right)^n_{j,k} \stackrel{\text{def}}{=} \frac{(-1)^q}{3}\left(s^{(q)}_3 - s^{(q)}_1\right). \tag{3.53}$$

Note that Eqs. (3.37)–(3.42) are equivalent to Eqs. (3.51) and (3.52).

The 2D *a* scheme is formed using Eqs. (3.51) and (3.52). It has been shown numerically that it is second order in accuracy for $u^n_{j,k}$, $(u_\zeta)^n_{j,k}$ and $(u_\eta)^n_{j,k}$ assuming that ν_ζ and ν_η are held constant in the process of mesh refinement (note: as a result of Eq. (3.22), the 2D *a* scheme is third order accuracy in $(u^+_\zeta)^n_{j,k}$ and $(u^+_\eta)^n_{j,k}$). Note that the superscript symbol "*a*" in $(u^{a+}_\zeta)^n_{j,k}$ and $(u^{a+}_\eta)^n_{j,k}$ is introduced to remind the reader that Eq. (3.52) is valid for the 2D *a* scheme.

The 2D *a* scheme shares with the 1D *a* scheme several nontraditional features. They are summarized in the following comments:

(a) As in the case of the 1D *a* scheme, the 2D *a* scheme also has the simplest stencil possible, i.e., a tetrahedron in 3D space-time with one vertex at the upper time level and the other three vertices at the lower time level.

(b) As in the case of the 1D *a* scheme, each of the six flux conservation conditions associated with the 2D *a* scheme, i.e., those given in Eq. (3.26), represents a relation among the marching variables associated with only two neighboring SEs.

(c) As in the case of the 1D *a* scheme, the 2D *a* scheme also is nondissipative if it is stable. It is shown in Section 7 of [7] that the 2D *a* scheme is neutrally stable if

$$|\nu_\zeta| < 1.5, \quad |\nu_\eta| < 1.5, \quad \text{and} \quad |\nu_\zeta + \nu_\eta| < 1.5. \tag{3.54}$$

As depicted in Fig. 13, the domain of stability defined by Eq. (3.54) is a hexagonal region in the ν_ζ-ν_η plane.

(d) It is shown in [10] that the 2D *a* scheme has the following property: i.e., for any $(j, k, n) \in \Omega$,

$$\mathbf{q}(j, k, n+1) \to \mathbf{q}(j, k, n) \text{ as } \Delta t \to 0 \tag{3.55}$$

if a_x, a_y, w, b, and h are held constant. Here $\mathbf{q}(j, k, n)$ is the column matrix formed by the three marching variables at the mesh point (j, k, n) [7]. The 1D *a* scheme also possesses a similar property, i.e., Eq. (2.19) in [2]. The above property usually is not shared by other schemes that use a mesh that is staggered in time, e.g., the Lax scheme [30, p. 74].

(e) As in the case of the 1D *a* scheme, the 2D *a* scheme is also a two-way marching scheme; i.e., Eqs. (3.37)–(3.42) can also be used to construct the backward time-marching version of the 2D *a* scheme [10].

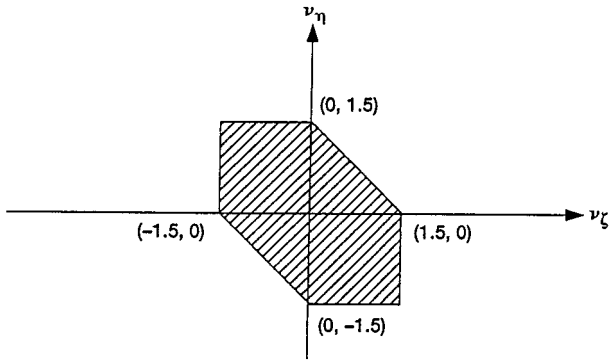

FIG. 13. The stability domain of the 2D a scheme.

Note that the 2D a scheme can also be expressed in terms of the marching variables and the coefficients tied to the coordinates (x, y). Here the coordinates (ζ, η) are introduced solely for the purpose of simplifying the current development (note: as an example, the proof given in Appendix D of [7] that Eq. (3.54) can be interpreted as the requirement that the physical domain of dependence of Eq. (3.1) be within the numerical domain of dependence would not be so simple if the coordinates (ζ, η) were not introduced). The essence of the 2D a scheme, and the schemes to be introduced in the following sections, is not dependent on the choice of the coordinates in terms of which of these schemes are expressed.

4. THE 2D a-ϵ SCHEME

In this section, the nondissipative 2D a scheme will be extended to become the dissipative 2D a-ϵ scheme.

To proceed, note that the CEs for the 2D a-ϵ scheme generally are not those associated with the 2D a scheme. Here only a single CE is associated with a mesh point $(j, k, n) \in \Omega$. This CE, denoted by $\mathrm{CE}(j, k, n)$, is the union of $\mathrm{CE}_r(j, k, n)$, $r = 1, 2, 3$. In other words,

$$CE(j,k,n) \stackrel{\text{def}}{=} [CE_1(j,k,n)] \cup [CE_2(j,k,n)] \cup [CE_3(j,k,n)]. \tag{4.1}$$

Instead of Eq. (3.10), here we assume the less stringent conservation condition

$$\oint_{S(CE(j,k,n))} \mathbf{h}^* \cdot d\mathbf{s} = 0. \tag{4.2}$$

Obviously, (i) E_3 can be filled with the new CEs, and (ii) the total flux leaving the boundary of any space-time region that is the union of any new CEs will also vanish.

Moreover, because of Eq. (4.1), Eq. (4.2) must be true if Eq. (3.10) is assumed. As a matter of fact, a direct evaluation of Eq. (4.2) reveals that it is equivalent to Eq. (3.51). As a result, Eq. (3.51) is shared by the 2D a scheme and 2D a-ϵ scheme. In this section, the 2D a-ϵ scheme will be constructed by modifying Eq. (3.52), the second equation in the a scheme. As a prerequisite, we shall first construct certain central-difference analogues of $\partial u/\partial\zeta$ and $\partial u/\partial\eta$.

To proceed, for any $(j, k, n) \in \Omega_q$, $q = 1, 2$, let

$$u'^{n}_{(j,k;q,r)} \stackrel{\text{def}}{=} \left(u + \frac{\Delta t}{2} u_t \right)^{n-1/2}_{(j,k;q,r)}, \quad r = 1, 2, 3. \tag{4.3}$$

By its definition, $u'^{n}_{(j,k;q,r)}$ is a Taylor series estimate of u at $((j, k; q, r), n)$. With the aid of Eqs. (3.18), (3.21), and (3.22), Eq. (4.3) implies that

$$u'^{n}_{(j,k;q,r)} = [u - 2(\nu_\zeta u^+_\zeta + \nu_\eta u^+_\eta)]^{n-1/2}_{(j,k;q,r)}. \tag{4.4}$$

For both $q = 1$ and $q = 2$, let P, Q, and R be the three points in the ζ-η-u space with their (i) ζ- and η-coordinates being those of the mesh points $((j, k; q, r), n - 1/2)$, $r = 1, 2, 3$, respectively, and (ii) their u-coordinates being $u'^{n}_{(j,k;q,r)}$, $r = 1, 2, 3$, respectively. It can be shown that [7], at any point on the plane containing points P, Q, and R, we have

$$\left(\frac{\partial u}{\partial \zeta} \right)_\eta = \left(u^c_\zeta \right)^n_{j,k}, \quad \text{and} \quad \left(\frac{\partial u}{\partial \eta} \right)_\zeta = \left(u^c_\eta \right)^n_{j,k}. \tag{4.5}$$

Here

$$\left(u^c_\zeta \right)^n_{j,k} \stackrel{\text{def}}{=} (-1)^q \left(u'^{n}_{(j,k;q,2)} - u'^{n}_{(j,k;q,1)} \right) / \Delta\zeta \tag{4.6}$$

and

$$\left(u^c_\eta \right)^n_{j,k} \stackrel{\text{def}}{=} (-1)^q \left(u'^{n}_{(j,k;q,3)} - u'^{n}_{(j,k;q,1)} \right) / \Delta\eta. \tag{4.7}$$

As a result of the above considerations, and the fact that the spatial projection of the mesh point $(j, k, n) \in \Omega_q$ on the $(n - 1/2)$th time level is the centroid of the triangle formed with the mesh points $((j, k; q, r), n - 1/2)$, $r = 1, 2, 3$, one concludes that $(u^c_\zeta)^n_{j,k}$ and $(u^c_\eta)^n_{j,k}$ are central-difference approximations of $\partial u/\partial\zeta$ and $\partial u/\partial\eta$, respectively, at the mesh point (j, k, n).

To proceed, for any $(j, k, n) \in \Omega$, let

$$\left(u^{c+}_\zeta \right)^n_{j,k} \stackrel{\text{def}}{=} \frac{\Delta\zeta}{6} \left(u^c_\zeta \right)^n_{j,k} \quad \text{and} \quad \left(u^{c+}_\eta \right)^n_{j,k} \stackrel{\text{def}}{=} \frac{\Delta\eta}{6} \left(u^c_\eta \right)^n_{j,k}. \tag{4.8}$$

Then the 2D a-ϵ scheme is formed by Eq. (3.51) and

$$(u^+_\zeta)^n_{j,k} = \left(u^{a+}_\zeta \right)^n_{j,k} + 2\epsilon \left(u^{c+}_\zeta - u^{a+}_\zeta \right)^n_{j,k} \tag{4.9}$$

and

$$(u^+_\eta)^n_{j,k} = \left(u^{a+}_\eta \right)^n_{j,k} + 2\epsilon \left(u^{c+}_\eta - u^{a+}_\eta \right)^n_{j,k}, \tag{4.10}$$

where ϵ is an adjustable parameter.

Note that the expression on the right side of Eq. (4.9) contains two parts. The first part is the nondissipative term $(u^{a+}_\zeta)^n_{j,k}$ (recall that the 2D a scheme is nondissipative). The second part is the product of 2ϵ and the difference between the dissipative central difference term $(u^{c+}_\zeta)^n_{j,k}$ and the nondissipative term $(u^{a+}_\zeta)^n_{j,k}$. Numerical dissipation is introduced by the

second part. The expression on the right side of Eq. (4.10) can also be interpreted similarly. Thus, numerical dissipation of the 2D a-ϵ scheme can be adjusted upward by increasing the value of ϵ.

Note that because the 2D a-ϵ scheme does not reduce to the 2D a scheme except in the special case $\epsilon = 0$, at each mesh point $(j, k, n) \in \Omega$, generally the 2D a-ϵ satisfies only the single conservation condition Eq. (4.2) rather than the three conservation conditions Eq. (3.10). However, because $(u_\zeta^{a+})_{j,k}^n$ and $(u_\eta^{a+})_{j,k}^n$ generally are present on the right sides of Eqs. (4.9) and (4.10), respectively, the 2D a-ϵ scheme generally will still be burdened with the cost of solving three conservation conditions at each mesh point. The exception occurs only for the special case $\epsilon = 1/2$ under which Eqs. (4.9) and (4.10) reduce to $(u_\zeta^+)_{j,k}^n = (u_\zeta^{c+})_{j,k}^n$ and $(u_\eta^+)_{j,k}^n = (u_\eta^{c+})_{j,k}^n$, respectively.

This section is concluded with the following remarks:

(a) The stability domain of the 2D a-ϵ scheme on the ν_ζ-ν_η plane is essentially that depicted in Fig. 13 if $0 \le \epsilon \le 1$ [7].

(b) It is explained in [7] that the 2D a-ϵ scheme with $\epsilon > 0$ is second order in accuracy for $u_{j,k}^n$ and first order in accuracy for $(u_\zeta)_{j,k}^n$ and $(u_\eta)_{j,k}^n$, assuming that ν_ζ, ν_η, and ϵ are held constant in the process of mesh refinement.

(c) A more advanced scheme, referred to as the 2D a-ϵ-α-β scheme, is described in [7]. This scheme is constructed by using a procedure similar to that used to construct the 2D Euler a-ϵ-α-β scheme which will be described in Section 5.

5. THE EULER SOLVERS

We consider a dimensionless form of the 2D unsteady Euler equations of a perfect gas. Let ρ, u, v, p, and γ be the mass density, x-velocity component, y-velocity component, static pressure, and constant specific heat ratio, respectively. Let

$$u_1 = \rho, \quad u_2 = \rho u, \quad u_3 = \rho v, \quad u_4 = p/(\gamma - 1) + \rho(u^2 + v^2)/2 \tag{5.1}$$

$$f_1^x = u_2, \quad f_1^y = u_3, \quad f_3^x = f_2^y = u_2 u_3/u_1 \tag{5.2}$$

$$f_2^x = (\gamma - 1)u_4 + (3 - \gamma)(u_2)^2/(2u_1) - (\gamma - 1)(u_3)^2/(2u_1) \tag{5.3}$$

$$f_4^x = \gamma u_2 u_4/u_1 - (1/2)(\gamma - 1)u_2\left[(u_2)^2 + (u_3)^2\right]/(u_1)^2 \tag{5.4}$$

$$f_3^y = (\gamma - 1)u_4 + (3 - \gamma)(u_3)^2/(2u_1) - (\gamma - 1)(u_2)^2/(2u_1) \tag{5.5}$$

and

$$f_4^y = \gamma u_3 u_4/u_1 - (1/2)(\gamma - 1)u_3\left[(u_2)^2 + (u_3)^2\right]/(u_1)^2. \tag{5.6}$$

Then the Euler equations can be expressed as

$$\frac{\partial u_m}{\partial t} + \frac{\partial f_m^x}{\partial x} + \frac{\partial f_m^y}{\partial y} = 0, \quad m = 1, 2, 3, 4. \tag{5.7}$$

Assuming smoothness of the physical solution, Eq. (5.7) is a result of the more fundamental conservation laws

$$\oint_{S(V)} \mathbf{h}_m \cdot d\mathbf{s} = 0, \quad m = 1, 2, 3, 4, \tag{5.8}$$

where

$$\mathbf{h}_m = \left(f_m^x,\ f_m^y, u_m \right), \quad m = 1, 2, 3, 4 \tag{5.9}$$

are the space-time mass, x-momentum component, y-momentum component, and energy current density vectors, respectively.

As a preliminary, let

$$f_{m,\ell}^x \stackrel{\text{def}}{=} \partial f_m^x / \partial u_\ell, \quad \text{and} \quad f_{m,\ell}^y \stackrel{\text{def}}{=} \partial f_m^y / \partial u_\ell, \quad m, \ell = 1, 2, 3, 4. \tag{5.10}$$

The Jacobian matrices, which are formed by $f_{m,\ell}^x$ and $f_{m,\ell}^y$, $m, \ell = 1, 2, 3, 4$, respectively, are given in [10].

Because f_m^x and f_m^y, $m = 1, 2, 3, 4$, are homogeneous functions of degree 1 [31, p. 11] in u_1, u_2, u_3, and u_4, we have

$$f_m^x = \sum_{\ell=1}^{4} f_{m,\ell}^x u_\ell, \quad \text{and} \quad f_m^y = \sum_{\ell=1}^{4} f_{m,\ell}^y u_\ell. \tag{5.11}$$

Note that Eq. (5.11) is not essential in the development of the CE/SE Euler solvers to be described in the following subsections. However, in certain instances, it will be used to recast some equations into more convenient forms.

Before proceeding, note that Section 2 of [7] is devoted to (i) reviewing and reformulating the 1D schemes described in [2] and (ii) filling a gap in the derivation of Eq. (4.28) in [2]. Not only does the reformulation enable the reader to see more clearly the structural similarity between the 1D solvers of Eq. (1.1) with $\mu = 0$ and their Euler counterparts, it also makes it easier for the reader to appreciate the consistency between the construction of the 1D CE/SE Euler solvers and that of the 2D Euler solvers to be described immediately.

5.1. *The 2D Euler a Scheme*

For any $(x, y, t) \in \text{SE}(j, k, n)$, $u_m(x, y, t)$, $f_m^x(x, y, t)$, $f_m^y(x, y, t)$, and $\mathbf{h}_m(x, y, t)$, respectively, are approximated by $u_m^*(x, y, t;\ j, k, n)$, $f_m^{x*}(x, y, t;\ j, k, n)$, $f_m^{y*}(x, y, t;\ j, k, n)$, and $\mathbf{h}_m^*(x, y, t;\ j, k, n)$. They will be defined shortly. Let

$$\begin{aligned} u_m^*(x, y, t;\ j, k, n) \stackrel{\text{def}}{=} & (u_m)_{j,k}^n + (u_{mx})_{j,k}^n (x - x_{j,k}) + (u_{my})_{j,k}^n (y - y_{j,k}) \\ & + (u_{mt})_{j,k}^n (t - t^n), \quad m = 1, 2, 3, 4, \end{aligned} \tag{5.12}$$

where $(u_m)_{j,k}^n$, $(u_{mx})_{j,k}^n$, $(u_{my})_{j,k}^n$, and $(u_{mt})_{j,k}^n$ are constants in $\text{SE}(j, k, n)$.

Let $(f_m^x)_{j,k}^n$, $(f_m^y)_{j,k}^n$, $(f_{m,\ell}^x)_{j,k}^n$, and $(f_{m,\ell}^y)_{j,k}^n$ denote the values of f_m^x, f_m^y, $f_{m,\ell}^x$, and $f_{m,\ell}^y$, respectively; when u_m, $m = 1, 2, 3, 4$, respectively, assume the values of $(u_m)_{j,k}^n$, $m = 1, 2, 3, 4$. For any $m = 1, 2, 3, 4$, let

$$\left(f_{mx}^x \right)_{j,k}^n \stackrel{\text{def}}{=} \sum_{\ell=1}^{4} \left(f_{m,\ell}^x \right)_{j,k}^n (u_{\ell x})_{j,k}^n. \tag{5.13}$$

Similarly $(f_{my}^x)_{j,k}^n$, $(f_{mt}^x)_{j,k}^n$, $(f_{mx}^y)_{j,k}^n$, $(f_{my}^y)_{j,k}^n$, and $(f_{mt}^y)_{j,k}^n$ are defined by replacing (i) both superscripts x in Eq. (5.13) with x or y and (ii) both subscripts x in Eq. (5.13) with x, y, or t.

Because (i)

$$\frac{\partial f_m^x}{\partial x} = \sum_{\ell=1}^{4} f_{m,\ell}^x \frac{\partial u_\ell}{\partial x}, \quad m = 1, 2, 3, 4 \tag{5.14}$$

and (ii) the expression on the right side of Eq. (5.13) is the numerical analogue of that on the right side of Eq. (5.14) at $(x_{j,k}, y_{j,k}, t^n)$, $(f_{mx}^x)_{j,k}^n$ will be interpreted as the numerical analogue of the value of $\partial f_m^x/\partial x$ at $(x_{j,k}, y_{j,k}, t^n)$. Similar interpretations will also be given to $(f_{my}^x)_{j,k}^n$, $(f_{mt}^x)_{j,k}^n$, $(f_{mx}^y)_{j,k}^n$, $(f_{my}^y)_{j,k}^n$, and $(f_{mt}^y)_{j,k}^n$. As a result, we define

$$\begin{aligned} f_m^{x*}(x, y, t; j, k, n) \stackrel{\text{def}}{=} & \left(f_m^x\right)_{j,k}^n + \left(f_{mx}^x\right)_{j,k}^n (x - x_{j,k}) + \left(f_{my}^x\right)_{j,k}^n (y - y_{j,k}) \\ & + \left(f_{mt}^x\right)_{j,k}^n (t - t^n), \quad m = 1, 2, 3, 4 \end{aligned} \tag{5.15}$$

and

$$\begin{aligned} f_m^{y*}(x, y, t; j, k, n) \stackrel{\text{def}}{=} & \left(f_m^y\right)_{j,k}^n + \left(f_{mx}^y\right)_{j,k}^n (x - x_{j,k}) + \left(f_{my}^y\right)_{j,k}^n (y - y_{j,k}) \\ & + \left(f_{mt}^y\right)_{j,k}^n (t - t^n), \quad m = 1, 2, 3, 4. \end{aligned} \tag{5.16}$$

Also, as an analogue to Eq. (5.9), we define

$$\mathbf{h}_m^*(x, y, t; j, k, n) \stackrel{\text{def}}{=} \left(f_m^{x*}(x, y, t; j, k, n),\ f_m^{y*}(x, y, t; j, k, n), u_m^*(x, y, t; j, k, n)\right), \quad m = 1, 2, 3, 4. \tag{5.17}$$

Note that, by their definitions, (i) $(f_m^x)_{j,k}^n$, $(f_m^y)_{j,k}^n$, $(f_{m,\ell}^x)_{j,k}^n$, and $(f_{m,\ell}^y)_{j,k}^n$ are functions of $(u_m)_{j,k}^n$, $m = 1, 2, 3, 4$; (ii) $(f_{mx}^x)_{j,k}^n$ and $(f_{mx}^y)_{j,k}^n$ are functions of $(u_m)_{j,k}^n$ and $(u_{mx})_{j,k}^n$, $m = 1, 2, 3, 4$; (iii) $(f_{my}^x)_{j,k}^n$ and $(f_{my}^y)_{j,k}^n$ are functions of $(u_m)_{j,k}^n$ and $(u_{my})_{j,k}^n$, $m = 1, 2, 3, 4$; and (iv) $(f_{mt}^x)_{j,k}^n$ and $(f_{mt}^y)_{j,k}^n$ are functions of $(u_m)_{j,k}^n$ and $(u_{mt})_{j,k}^n$, $m = 1, 2, 3, 4$.

Moreover, we assume that, for any $(x, y, t) \in \mathrm{SE}(j, k, n)$, and any $m = 1, 2, 3, 4$,

$$\frac{\partial u_m^*(x, y, t; j, k, n)}{\partial t} + \frac{\partial f_m^{x*}(x, y, t; j, k, n)}{\partial x} + \frac{\partial f_m^{y*}(x, y, t; j, k, n)}{\partial y} = 0. \tag{5.18}$$

Note that Eq. (5.18) is the numerical analogue of Eq. (5.7). With the aid of Eqs. (5.12), (5.15), (5.16), and the definitions of $(f_{mx}^x)_{j,k}^n$ and $(f_{my}^y)_{j,k}^n$, Eq. (5.18) implies that, for any $m = 1, 2, 3, 4$,

$$(u_{mt})_{j,k}^n = -\left(f_{mx}^x\right)_{j,k}^n - \left(f_{my}^y\right)_{j,k}^n = -\sum_{\ell=1}^{4} \left[f_{m,\ell}^x u_{\ell x} + f_{m,\ell}^y u_{\ell y}\right]_{j,k}^n. \tag{5.19}$$

Thus, $(u_{mt})_{j,k}^n$ is a function of $(u_m)_{j,k}^n$, $(u_{mx})_{j,k}^n$, and $(u_{my})_{j,k}^n$. From this result and the facts stated following Eq. (5.17), one concludes that the only independent discrete variables that need to be solved for in the current marching scheme are $(u_m)_{j,k}^n$, $(u_{mx})_{j,k}^n$, and $(u_{my})_{j,k}^n$.

Consider the conservation elements depicted in Figs. 9a and 10a. The Euler counterpart to Eq. (3.10) is

$$\oint_{S(CE_r(j,k,n))} \mathbf{h}_m^* \cdot d\mathbf{s} = 0, \quad r = 1, 2, 3, \quad m = 1, 2, 3, 4, \tag{5.20}$$

where $(j, k, n) \in \Omega$.

To proceed further, we shall introduce the Euler counterparts of Eqs. (3.16), (3.17), (3.21), and (3.22). For any $(j, k, n) \in \Omega$, let

$$\begin{pmatrix} \left(f^{\zeta}_{m,\ell}\right)^n_{j,k} \\ \left(f^{\eta}_{m,\ell}\right)^n_{j,k} \end{pmatrix} \stackrel{\text{def}}{=} T^{-1} \begin{pmatrix} \left(f^{x}_{m,\ell}\right)^n_{j,k} \\ \left(f^{y}_{m,\ell}\right)^n_{j,k} \end{pmatrix}, \quad m, \ell = 1, 2, 3, 4 \tag{5.21}$$

and

$$\begin{pmatrix} (u_{m\zeta})^n_{j,k} \\ (u_{m\eta})^n_{j,k} \end{pmatrix} \stackrel{\text{def}}{=} T^{t} \begin{pmatrix} (u_{mx})^n_{j,k} \\ (u_{my})^n_{j,k} \end{pmatrix}, \quad m = 1, 2, 3, 4. \tag{5.22}$$

The normalized counterparts of those parameters defined in Eqs. (5.21) and (5.22) are

$$\left(f^{\zeta+}_{m,\ell}\right)^n_{j,k} \stackrel{\text{def}}{=} \frac{3\Delta t}{2\Delta\zeta}\left(f^{\zeta}_{m,\ell}\right)^n_{j,k}, \quad \text{and} \quad \left(f^{\eta+}_{m,\ell}\right)^n_{j,k} \stackrel{\text{def}}{=} \frac{3\Delta t}{2\Delta\eta}\left(f^{\eta}_{m,\ell}\right)^n_{j,k} \tag{5.23}$$

and

$$(u^{+}_{m\zeta})^n_{j,k} \stackrel{\text{def}}{=} \frac{\Delta\zeta}{6}(u_{m\zeta})^n_{j,k}, \quad \text{and} \quad (u^{+}_{m\eta})^n_{j,k} \stackrel{\text{def}}{=} \frac{\Delta\eta}{6}(u_{m\eta})^n_{j,k}. \tag{5.24}$$

To simplify the following development, we may strip from every discrete variable in an equation (or in a statement) its indices j, k, and n if all variables are associated with the same mesh point $(j, k, n) \in \Omega$. Let $\mathbf{u}$, $\mathbf{u}_t$, $\mathbf{u}^+_\zeta$, and $\mathbf{u}^+_\eta$, respectively, be the 4×1 column matrices formed by u_m, u_{mt}, $u^+_{m\zeta}$, and $u^+_{m\eta}$, $m = 1, 2, 3, 4$. Let $F^{\zeta+}$ and $F^{\eta+}$, respectively, denote the 4×4 matrices formed by $f^{\zeta+}_{m,\ell}$ and $f^{\eta+}_{m,\ell}$, $m, \ell = 1, 2, 3, 4$. Let I be the 4×4 identity matrix. Let the 4×4 coefficient matrices $\Sigma^{(q)\pm}_{rs}$, $q = 1, 2$ and $r, s = 1, 2, 3$, be defined using a set of equations that are exactly identical to Eqs. (3.27)–(3.35) except that

(1) each $\sigma^{(q)\pm}_{rs}$ be replaced by its Euler image $\Sigma^{(q)\pm}_{rs}$ and

(2) ν_ζ, ν_η, and any real number ϕ, be replaced by their Euler images $F^{\zeta+}$, $F^{\eta+}$, and ϕI, respectively.

Note that matrix multiplication is not commutative. Thus, in applying the substitution rule (2), the order of factors in any product in Eqs. (3.27)–(3.35) should not be altered.

As will be shown, under the above and other rules of substitution to be given later, many parameters, variables, and equations introduced in Sections 3 and 4 have their designated Euler images. It can be shown easily that the Euler images of Eqs. (3.49) and (3.50) are also valid. Note that, for simplicity, hereafter the Euler image of an equation such as Eq. (3.49) may be denoted as Eq. (EI-3.49).

Equation (5.20) is evaluated in Appendix C of [7]. This evaluation is greatly simplified by the fact that $u^*_m(x, y, t; j, k, n)$, $f^{x*}_m(x, y, t; j, k, n)$, and $f^{y*}_m(x, y, t; j, k, n)$ are linear in x, y, and t (see Eqs. (5.12), (5.15), and (5.16)). As a result of that fact, Eq. (5.17) implies that, for any $r = 1, 2, 3$, the total flux of $\mathbf{h}^*_m$ leaving $\text{CE}_r(j, k, n)$ through any one of the six quadrilaterals that form its boundary is equal to the scalar product of the vector $\mathbf{h}^*_m$ evaluated at the centroid of the quadrilateral and the surface vector (defined in Section 3) of the quadrilateral. Let $(j, k, n) \in \Omega_q$. Then, with the aid of Eq. (5.11), for any pair of q and r ($q = 1, 2$ and $r = 1, 2, 3$), the final evaluation results with $m = 1, 2, 3, 4$ can be combined

into the matrix form

$$\left[\Sigma_{r1}^{(q)+}\mathbf{u}+\Sigma_{r2}^{(q)+}\mathbf{u}_\zeta^+ +\Sigma_{r3}^{(q)+}\mathbf{u}_\eta^+\right]_{j,k}^n = \left[\Sigma_{r1}^{(q)-}\mathbf{u}+\Sigma_{r2}^{(q)-}\mathbf{u}_\zeta^+ +\Sigma_{r3}^{(q)-}\mathbf{u}_\eta^+\right]_{(j,k;q,r)}^{n-1/2}. \quad (5.25)$$

Equation (5.25) is the Euler image of Eq. (3.26) under the substitution rules (1) and

(3) u, u_t, u_ζ^+, and u_η^+ be replaced by their Euler images $\mathbf{u}$, $\mathbf{u}_t$, $\mathbf{u}_\zeta^+$, and $\mathbf{u}_\eta^+$, respectively.

Note that (i) for each $(j,k,n)\in\Omega_q$, $q=1,2$, Eq. (5.25) represents a system of three matrix equations while Eq. (3.26) represents a system of three scalar equations; (ii) matrix multiplication is not commutative; and (iii) the coefficient matrices $\Sigma_{rs}^{(q)\pm}$ are functions of $\mathbf{u}_{j,k}^n$ while the coefficients $\sigma_{rs}^{(q)\pm}$ are constants. As a result, in spite of the fact that Eq. (5.25) shares with Eq. (3.26) the same algebraic structure, as will be shown shortly, the algebraic structure of the solution to Eq. (5.25) is more complex than that of Eq. (3.26).

Using an argument similar to that leads to Eq. (3.51), one concludes that the Euler image of Eq. (3.51) is also valid.

Note that, for any $(j,k,n)\in\Omega_q$, the matrices $(\Sigma_{r1}^{(q)+})_{j,k}^n$, $r=1,2,3$, are known functions of $\mathbf{u}_{j,k}^n$. Thus they can be evaluated after the latter is evaluated using Eq. (EI-3.51). Assuming the existence of the inverse of each of the matrices $(\Sigma_{r1}^{(q)+})_{j,k}^n$, one can also evaluate $\mathbf{S}_r^{(q)}$ ($q=1,2$ and $r=1,2,3$), where

$$\mathbf{S}_r^{(q)} \stackrel{\text{def}}{=} \left[\left(\Sigma_{r1}^{(q)+}\right)_{j,k}^n\right]^{-1} \times \left[\Sigma_{r1}^{(q)-}\mathbf{u}+\Sigma_{r2}^{(q)-}\mathbf{u}_\zeta^+ +\Sigma_{r3}^{(q)-}\mathbf{u}_\eta^+\right]_{(j,k;q,r)}^{n-1/2}. \quad (5.26)$$

Note that the above inverse must exist if the local *CFL* number at (j,k,n) is less than $2/3$ (see a theorem in Appendix D.3 in [7]). Moreover, numerical evidence suggests that generally it is safe to make the existence assumption as long as the local *CFL* number <1.

By multiplying Eq. (5.25) from the left with

$$\left[\left(\Sigma_{r1}^{(q)+}\right)_{j,k}^n\right]^{-1}$$

repeatedly with all possible pairs of q and r, and using Eqs. (EI-3.27)–(EI-3.35) and Eq. (5.26), one obtains a set of equations [7] that are the Euler images of Eqs. (3.37)–(3.42) under the substitution rules (2), (3), and

(4) each $s_r^{(q)}$ be replaced by its Euler image $\mathbf{S}_r^{(q)}$.

Let $\mathbf{u}_\zeta^{a+}$ and $\mathbf{u}_\eta^{a+}$ be defined using the Euler image of Eq. (3.53) under the substitution rules (4) and

(5) u_ζ^{a+} and u_η^{a+} be replaced by their Euler images $\mathbf{u}_\zeta^{a+}$ and $\mathbf{u}_\eta^{a+}$, respectively.

Then the validity of Eq. (EI-3.52) follows from Eqs. (EI-3.37)–(EI-3.42). The 2D Euler *a* scheme is formed by Eqs. (EI-3.51) and (EI-3.52). This scheme is a two-way marching scheme in the sense that the conservation conditions Eq. (5.20) can also be used to construct its backward time marching version.

Note that the matrices $(\Sigma_{rs}^{(q)+})_{j,k}^n$ are nonlinear functions of $\mathbf{u}_{j,k}^n$. Thus, for each $(j,k,n)\in\Omega_q$, $q=1,2$, Eq. (5.25) represents a system of three nonlinear matrix equations. Generally one would not expect that Eq. (5.25) can be solved through a noniterative explicit procedure as described above. The key to the unexpectedly simple solution procedure is the fact that $\mathbf{u}_{j,k}^n$ can be evaluated explicitly using Eq. (EI-3.51). In the following, we will explain how Eq. (EI-3.51) arises and give a hint on how to preserve the simplicity of the current solution procedure in case an irregular spatial mesh is used.

Note that, because of Eq. (4.1),

$$\oint_{S(CE(j,k,n))} \mathbf{h}_m^* \cdot d\mathbf{s} = 0, \quad (j,k,n) \in \Omega \tag{5.27}$$

is the direct result of Eq. (5.20). According to Eq. (4.1), $CE(j,k,n)$ is the hexagonal cylinder $A'B'C'D'E'F'ABCDEF$ depicted in Figs. 9a and 10a. Except for the top face $A'B'C'D'E'F'$, the other boundaries of this cylinder are the subsets of three solution elements at the $(n-1/2)$th time level. Thus, for any $m=1,2,3,4$, the flux of $\mathbf{h}_m^*$ leaving $CE(j,k,n)$ through all the boundaries except the top face can be evaluated in terms of the marching variables at the $(n-1/2)$th time level. On the other hand, because the top face is a subset of $\mathrm{SE}(j,k,n)$, the flux leaving there is a function of the marching variables associated with the mesh point (j,k,n). Furthermore, because the outward normal to the top face has no spatial component, the total flux of $\mathbf{h}_m^*$ leaving $CE(j,k,n)$ through the top face is the surface integral of u_m^* over the top face. Because the center of $\mathrm{SE}(j,k,n)$ coincides with the center of the top face, it is easy to see that the first-order terms in Eqs. (5.12) do not contribute to the total flux leaving the top face. It follows that the total flux leaving the top face is a function of $(u_m)_{j,k}^n$ only. As a result of the above considerations, $\mathbf{u}_{j,k}^n$ can be determined in terms of the marching variables at the $(n-1/2)$th time level by using Eq. (5.27) only. Equation (EI-3.51) is the direct result of Eq. (5.27).

From the above discussion, it becomes obvious that, in case an irregular spatial mesh is used [12, 13], $\mathbf{u}_{j,k}^n$ can still be expressed as a simple function of the marching variables at the $(n-1/2)$th time level as long as the mesh point (j,k,n) is located at the center of the top face of $CE(j,k,n)$. Note that in this case the three top faces of $CE_r(j,k,n)$, $r=1,2,3$, generally do not meet at the mesh point (j,k,n).

5.2. *The 2D Euler a-ϵ Scheme*

Equation (5.27) is assumed in the 2D Euler *a*-ϵ scheme. As a result, Eq. (EI-3.51) is also applicable to the new scheme.

To construct the rest of the scheme, consider any $(j,k,n) \in \Omega_q$ and any $m=1,2,3,4$. Let $(u'_m)_{(j,k;q,r)}^n$, $(u_{m\zeta}^c)_{j,k}^n$, and $(u_{m\eta}^c)_{j,k}^n$ be defined by a set of equations identical to Eqs. (4.3), (4.6), and (4.7) except that the symbols u', u, u_t, u_ζ^c, and u_η^c in the latter equations are replaced, respectively, by the symbols (u'_m), u_m, u_{mt}, $u_{m\zeta}^c$, and $u_{m\eta}^c$ in the former equations. Furthermore, let $(u_{m\zeta}^{c+})_{j,k}^n$ and $(u_{m\eta}^{c+})_{j,k}^n$ be defined using an equation that is identical to Eq. (4.8) except that the symbols u_ζ^{c+}, u_ζ^c, u_η^{c+}, and u_η^c in the latter equation are replaced, respectively, by the symbols $u_{m\zeta}^{c+}$, $u_{m\zeta}^c$, $u_{m\eta}^{c+}$, and $u_{m\eta}^c$ in the former equation.

Moreover, let $\mathbf{u}'$, $\mathbf{u}_\zeta^c$, $\mathbf{u}_\eta^c$, $\mathbf{u}_\zeta^{c+}$, and $\mathbf{u}_\eta^{c+}$, respectively, denote the 4×1 column matrices formed by u'_m, $u_{m\zeta}^c$, $u_{m\eta}^c$, $u_{m\zeta}^{c+}$, and $u_{m\eta}^{c+}$, $m=1,2,3,4$. Then one can obtain a set of equations [7] that are the Euler images of Eqs. (4.3), (4.4), and (4.6)–(4.10) under the substitution rules (2), (3), (5), and

(6) u', u_ζ^c, u_η^c, u_ζ^{c+}, and u_η^{c+} be replaced by their Euler images $\mathbf{u}'$, $\mathbf{u}_\zeta^c$, $\mathbf{u}_\eta^c$, $\mathbf{u}_\zeta^{c+}$, and $\mathbf{u}_\eta^{c+}$, respectively.

Note that it should be understood that the parameter ϵ in Eqs. (4.9) and (4.10) also appears as the same scalar (not ϵI as required by the rule (2)) in Eqs. (EI-4.9) and (EI-4.10).

The 2D Euler *a*-ϵ scheme is formed by Eqs. (EI-3.51), (EI-4.9), and (EI-4.10) for any $(j,k,n) \in \Omega_q$.

5.3. *The 2D Euler a-ϵ-α-β Scheme*

If discontinuities are present in a numerical solution, the above Euler schemes are not equipped to suppress numerical wiggles that generally appear near these discontinuities. In the following, we shall describe a remedy for this deficiency.

As a preliminary, for any $(j, k, n) \in \Omega_q$, any $m = 1, 2, 3, 4$, and any $r = 1, 2, 3$, let

$$x_{m,r} \stackrel{\text{def}}{=} (-1)^q \left[(u_m)^n_{j,k} - (u'_m)^n_{(j,k;q,r)} \right] \tag{5.28}$$

$$\left(u^{(r)}_{m\zeta}\right)^n_{j,k} \stackrel{\text{def}}{=} g^{(r)}_\zeta(x_{m,1}, x_{m,2}, x_{m,3}), \quad \left(u^{(r)}_{m\eta}\right)^n_{j,k} \stackrel{\text{def}}{=} g^{(r)}_\eta(x_{m,1}, x_{m,2}, x_{m,3}) \tag{5.29}$$

$$\left(u^{(r)}_{mx}\right)^n_{j,k} \stackrel{\text{def}}{=} g^{(r)}_x(x_{m,1}, x_{m,2}, x_{m,3}), \quad \left(u^{(r)}_{my}\right)^n_{j,k} \stackrel{\text{def}}{=} g^{(r)}_y(x_{m,1}, x_{m,2}, x_{m,3}). \tag{5.30}$$

Here $g^{(r)}_\zeta$, $g^{(r)}_\eta$, $g^{(r)}_x$, and $g^{(r)}_y$, $r = 1, 2, 3$, are the functions defined by (x_1, x_2, and x_3 are any real numbers)

$$g^{(1)}_\zeta(x_1, x_2, x_3) \stackrel{\text{def}}{=} -(2x_2 + x_3)/\Delta\zeta, \quad g^{(1)}_\eta(x_1, x_2, x_3) \stackrel{\text{def}}{=} -(x_2 + 2x_3)/\Delta\eta \tag{5.31}$$

$$g^{(2)}_\zeta(x_1, x_2, x_3) \stackrel{\text{def}}{=} (2x_1 + x_3)/\Delta\zeta, \quad g^{(2)}_\eta(x_1, x_2, x_3) \stackrel{\text{def}}{=} (x_1 - x_3)/\Delta\eta \tag{5.32}$$

$$g^{(3)}_\zeta(x_1, x_2, x_3) \stackrel{\text{def}}{=} (x_1 - x_2)/\Delta\zeta, \quad g^{(3)}_\eta(x_1, x_2, x_3) \stackrel{\text{def}}{=} (2x_1 + x_2)/\Delta\eta \tag{5.33}$$

$$g^{(1)}_x(x_1, x_2, x_3) \stackrel{\text{def}}{=} -\frac{3}{2w}(x_2 + x_3), \quad g^{(1)}_y(x_1, x_2, x_3) \stackrel{\text{def}}{=} \frac{(3b + w)x_2 + (3b - w)x_3}{2wh} \tag{5.34}$$

$$g^{(2)}_x(x_1, x_2, x_3) \stackrel{\text{def}}{=} \frac{3x_1}{2w}, \quad g^{(2)}_y(x_1, x_2, x_3) \stackrel{\text{def}}{=} -\frac{(3b + w)x_1 + 2wx_3}{2wh} \tag{5.35}$$

$$g^{(3)}_x(x_1, x_2, x_3) \stackrel{\text{def}}{=} \frac{3x_1}{2w}, \quad g^{(3)}_y(x_1, x_2, x_3) \stackrel{\text{def}}{=} \frac{(w - 3b)x_1 + 2wx_2}{2wh}. \tag{5.36}$$

To proceed further, for any $(j, k, n) \in \Omega_q$, $q = 1, 2$, consider any fixed value of $m = 1, 2, 3, 4$. Let P_m, Q_m, and R_m be the three points in the ζ-η-u space with (i) their ζ- and η-coordinates being those of the mesh points $((j, k; q, r), n - 1/2)$, $r = 1, 2, 3$, respectively, and (ii) their u-coordinates being $(u'_m)^n_{(j,k;q,r)}$, $r = 1, 2, 3$, respectively. Let O_m denote the point in the ζ-η-u space with the coordinates $(j\Delta\zeta, k\Delta\eta, (u_m)^n_{j,k})$. Let planes 1, 2, and 3, respectively, be the planes containing the following trios of points: (i) points O_m, Q_m, and R_m; (ii) points O_m, R_m, and P_m; and (iii) points O_m, P_m, and Q_m. Then it can be shown that [7], at any point on plane r, $r = 1, 2, 3$, we have

$$\left(\frac{\partial u}{\partial \zeta}\right)_\eta = \left(u^{(r)}_{m\zeta}\right)^n_{j,k}, \quad \left(\frac{\partial u}{\partial \eta}\right)_\zeta = \left(u^{(r)}_{m\eta}\right)^n_{j,k} \tag{5.37}$$

and

$$\left(\frac{\partial u}{\partial x}\right)_y = \left(u^{(r)}_{mx}\right)^n_{j,k}, \quad \left(\frac{\partial u}{\partial y}\right)_x = \left(u^{(r)}_{my}\right)^n_{j,k}. \tag{5.38}$$

Thus, at any point on plane r, $r = 1, 2, 3$, we have

$$|\nabla u| = (\theta_{mr})^n_{j,k} \stackrel{\text{def}}{=} \left[\sqrt{\left(u^{(r)}_{mx}\right)^2 + \left(u^{(r)}_{my}\right)^2} \right]^n_{j,k}. \tag{5.39}$$

Note that, by definition, $(\theta_{mr})^n_{j,k}$, $r = 1, 2, 3$, are scalars. For readers who are not familiar with tensor analysis, note that $(\theta_{mr})^n_{j,k}$ would not be a scalar and therefore the first equality sign in Eq. (5.39) would not be valid if $u^{(r)}_{mx}$ and $u^{(r)}_{my}$ in the same equation, respectively, are replaced by $u^{(r)}_{m\zeta}$ and $u^{(r)}_{m\eta}$.

For any $(j, k, n) \in \Omega$, let

$$u^{(r)+}_{m\zeta} \stackrel{\text{def}}{=} \frac{\Delta\zeta}{6} u^{(r)}_{m\zeta}, \quad u^{(r)+}_{m\eta} \stackrel{\text{def}}{=} \frac{\Delta\eta}{6} u^{(r)}_{m\eta}. \tag{5.40}$$

Then it can be shown that [7]

$$u^{c+}_{m\zeta} = \frac{1}{3}\left[u^{(1)+}_{m\zeta} + u^{(2)+}_{m\zeta} + u^{(3)+}_{m\zeta}\right], \quad u^{c+}_{m\eta} = \frac{1}{3}\left[u^{(1)+}_{m\eta} + u^{(2)+}_{m\eta} + u^{(3)+}_{m\eta}\right]; \tag{5.41}$$

i.e., $u^{c+}_{m\zeta}(u^{c+}_{m\eta})$ is the simple average of $u^{(r)+}_{m\zeta}(u^{(r)+}_{m\eta})$, $r = 1, 2, 3$.

By using an argument similar to that used to justify the introduction of a special weighted average defined by Eqs. (4.38) and (4.39) in [2], two weighted averages, respectively, of $u^{(r)+}_{m\zeta}$ and $u^{(r)+}_{m\eta}$, $r = 1, 2, 3$, are defined here by (α is any number ≥ 0)

$$u^{w+}_{m\zeta} \stackrel{\text{def}}{=} \begin{cases} 0, & \text{if } \theta_{m1} = \theta_{m2} = \theta_{m3} = 0 \\ \dfrac{(\theta_{m2}\theta_{m3})^\alpha u^{(1)+}_{m\zeta} + (\theta_{m3}\theta_{m1})^\alpha u^{(2)+}_{m\zeta} + (\theta_{m1}\theta_{m2})^\alpha u^{(3)+}_{m\zeta}}{(\theta_{m1}\theta_{m2})^\alpha + (\theta_{m2}\theta_{m3})^\alpha + (\theta_{m3}\theta_{m1})^\alpha}, & \text{otherwise} \end{cases} \tag{5.42}$$

and a similar definition in which all the subscripts ζ in Eq. (5.42) are replaced by η. Obviously $u^{w+}_{m\zeta} = u^{c+}_{m\zeta}$ and $u^{w+}_{m\eta} = u^{c+}_{m\eta}$ if $\alpha = 0$. Note that, to avoid dividing by zero, in practice a small positive number such as 10^{-60} may be added to the denominators on the right side of Eq. (5.42).

Note that the denominator in Eq. (5.42) vanishes if $\alpha > 0$ and any two of θ_{m1}, θ_{m2}, and θ_{m3} vanish. Thus, consistency of Eq. (5.42) requires proof of the proposition $\theta_{m1} = \theta_{m2} = \theta_{m3} = 0$, if any two of θ_{m1}, θ_{m2}, and θ_{m3} vanish. The proof is given in [7]. Also note that, as a result of the above definitions, it can be shown that [7]

$$u^{w+}_{m\zeta} = u^{c+}_{m\zeta} \quad \text{and} \quad u^{w+}_{m\eta} = u^{c+}_{m\eta}, \quad \text{if } \theta_{m1} = \theta_{m2} = \theta_{m3}. \tag{5.43}$$

Let $\mathbf{u}^{w+}_{\zeta}(\mathbf{u}^{w+}_{\eta})$ be the column matrix formed by $u^{w+}_{m\zeta}(u^{w+}_{m\eta})$, $m = 1, 2, 3, 4$. Then, for any $(j, k, n) \in \Omega$, the 2D Euler a-ϵ-α-β scheme is defined by Eq. (EI-3.51) and

$$(\mathbf{u}^{+}_{\zeta})^n_{j,k} = \left(\mathbf{u}^{a+}_{\zeta}\right)^n_{j,k} + 2\epsilon\left(\mathbf{u}^{c+}_{\zeta} - \mathbf{u}^{a+}_{\zeta}\right)^n_{j,k} + \beta\left(\mathbf{u}^{w+}_{\zeta} - \mathbf{u}^{c+}_{\zeta}\right)^n_{j,k} \tag{5.44}$$

and

$$(\mathbf{u}^{+}_{\eta})^n_{j,k} = \left(\mathbf{u}^{a+}_{\eta}\right)^n_{j,k} + 2\epsilon\left(\mathbf{u}^{c+}_{\eta} - \mathbf{u}^{a+}_{\eta}\right)^n_{j,k} + \beta\left(\mathbf{u}^{w+}_{\eta} - \mathbf{u}^{c+}_{\eta}\right)^n_{j,k}. \tag{5.45}$$

Here (i) ϵ and β are adjustable parameters; and (ii) $\mathbf{u}^{w+}_{\zeta}$ and $\mathbf{u}^{w+}_{\eta}$ are implicitly dependent on the adjustable parameter α. The scheme reduces to the 2D Euler a-ϵ scheme if $\beta = 0$ or $\alpha = 0$. It further reduces to the 2D Euler a scheme if, in addition, $\epsilon = 0$. Note that a discussion on how to choose the values of the parameters ϵ, α, and β will be given later in this section.

Note that numerical dissipation is added to the 2D Euler a-ϵ-α-β not through the main equation Eq. (EI-3.51) (which is equivalent to the conservation condition Eq. (5.27)). Rather it is introduced through two secondary equations which evaluate spatial derivatives. We suspect that this special feature, which is common to all CE/SE schemes, contributes to the accuracy of the CE/SE method.

Furthermore, note that the numerical dissipation introduced can be divided into two different types. Numerical dissipation of ϵ-type, i.e., that results from adding the second term to the right side of each of Eqs. (5.44) and (5.45), generally is very effective in damping out numerical instabilities that arise from the smooth region of a solution. But it is less effective in suppressing numerical wiggles that often occur near a discontinuity. On the other hand, numerical dissipation of α-β-type, i.e., that results from adding the third term, is very effective in suppressing numerical wiggles. Moreover, because, for each $m = 1, 2, 3, 4$, θ_{m1}, θ_{m2}, and θ_{m3} are nearly equal in the smooth region, Eq. (5.43) implies that $(\mathbf{u}_\zeta^{w+})_{j,k}^n$ and $(\mathbf{u}_\zeta^{c+})_{j,k}^n$ are also nearly equal there. As a result, numerical dissipation of α-β-type has very slight effect in the smooth region.

According to Eq. (5.26), at each mesh point $\in \Omega_q$, $q = 1, 2$, implementation of the above Euler schemes generally requires inverting three matrices (corresponding to $r = 1, 2, 3$). As a result, the schemes may be referred to as locally implicit. In the following, we shall describe how these schemes can be simplified and become completely explicit.

5.4. *The Simplified 2D Euler Schemes*

Equation (5.27) is assumed in the simplified schemes. As a result, Eq. (EI-3.51) is also applicable to the new schemes.

To construct the rest of the simplified schemes, we assume that the coefficient matrices $\Sigma_{r1}^{(q)+}$ vary only slightly among neighboring mesh points. Thus,

$$\left(\Sigma_{r1}^{(q)+}\right)_{j,k}^{n} \approx \left(\Sigma_{r1}^{(q)+}\right)_{(j,k;q,r)}^{n-1/2}. \tag{5.46}$$

Note that, according to extensive numerical evidence, the above approximation generally is accurate for subsonic, transonic, and supersonic flows as long as the mesh intervals and time-step size used are small enough. With the aid of Eqs. (EI-3.27)–(EI-3.35), a substitution Eq. (5.46) into Eq. (5.26) reveals that [7]

$$\mathbf{S}_r^{(q)} \approx \mathbf{s}_r^{(q)}, \quad q = 1, 2; \quad r = 1, 2, 3, \tag{5.47}$$

where $\mathbf{s}_r^{(q)}$ are defined using a set of equations that are exactly identical to Eqs. (3.43)–(3.48) except that $s_r^{(q)}$, u_ζ^+, u_η^+, ν_ζ, ν_η, and any real number ϕ are replaced by $\mathbf{s}_r^{(q)}$, $\mathbf{u}_\zeta^+$, $\mathbf{u}_\eta^+$, $F^{\zeta+}$, $F^{\eta+}$, and ϕI, respectively, using the substitution rules (2), (3), and

(4a) each $s_r^{(q)}$ be replaced by its alternative Euler image $\mathbf{s}_r^{(q)}$.

Note that, according to (4), $\mathbf{S}_r^{(q)}$ is also a Euler image of $s_r^{(q)}$. Thus, to avoid confusion, hereafter $\mathbf{s}_r^{(q)}$ is referred to as the alternative Euler image of $s_r^{(q)}$.

Furthermore, as a result of Eqs. (5.47), $\mathbf{u}_\zeta^{a'+}$ and $\mathbf{u}_\eta^{a'+}$ are defined using the alternative Euler image of Eq. (3.53) under the rules (4a) and

(5a) u_ζ^{a+} and u_η^{a+} be replaced by their alternative Euler images $\mathbf{u}_\zeta^{a'+}$ and $\mathbf{u}_\eta^{a'+}$, respectively.

The simplified schemes differ from the original schemes only in the fact that $\mathbf{u}_\zeta^{a+}$ and $\mathbf{u}_\eta^{a+}$ in the latter schemes, respectively, are replaced by $\mathbf{u}_\zeta^{a'+}$ and $\mathbf{u}_\eta^{a'+}$ in the former schemes. Note that the Euler schemes presented in [2] are the 1D counterparts of the current simplified schemes. The 1D counterparts of the full Euler schemes are described in [7].

5.5. *Remarks on the Parameters ϵ, α, and β*

According to numerical evidence and the analysis given in Section 7 of [7], stability of the current Euler solvers requires that (i) $0 \le \epsilon \le 1$, (ii) $\beta \ge 0$, (iii) $\alpha \ge 0$, and (iv) the maximal *CFL* number ≤ 1. Numerical evidence also suggests that the numerical dissipation introduced generally increases with the value of ϵ, α, and β.

Let $\epsilon = 1/2$ and $\beta = 1$. Then the 2D Euler a-ϵ-α-β scheme and its simplified version reduce to the same scheme. For any $(j, k, n) \in \Omega$, the reduced scheme is formed by Eq. (EI-3.51) and

$$(\mathbf{u}_\zeta^+)_{j,k}^n = \left(\mathbf{u}_\zeta^{w+}\right)_{j,k}^n, \quad \text{and} \quad (\mathbf{u}_\eta^+)_{j,k}^n = \left(\mathbf{u}_\eta^{w+}\right)_{j,k}^n. \tag{5.48}$$

The above scheme is one of the simplest among the 2D Euler solvers known to the authors. The value of α is the only adjustable parameter allowed in this scheme. Generally, with the choice of $\alpha = 1$ or $\alpha = 2$, the numerical dissipation introduced is sufficient to suppress numerical wiggles. Because it is totally explicit and has the simplest stencil, the scheme is also highly compatible with parallel computing. Furthermore, it will be shown in Section 7 that, in broad applications, the scheme can accurately capture shocks and contact discontinuities with high resolution and no numerical oscillations.

Note that, with ϵ, α, and β being held constant, numerical dissipation associated with the 2D Euler a-ϵ-α-β scheme (and its simplified version) at a mesh point (j, k, n) tends to increase as the local *CFL* number $\nu_{j,k}^n$ decreases. To compensate for this effect, ϵ and β in Eqs. (5.44) and (5.45), respectively, may be replaced by $\epsilon(\nu_{j,k}^n)$ and $\beta(\nu_{j,k}^n)$, where $\epsilon(x)$ and $\beta(x)$, $0 \le x \le 1$, are monotonically increasing functions of x with $\epsilon(0) = 0$ and $\beta(0) = 0$. Note that:

(a) It is shown in Figs. 12–14 of [2] that, with the choice

$$\epsilon(x) = 0.5\, x \exp(1 - x) \quad \text{and} \quad \beta(x) = \sqrt{x}, \quad 0 \le x \le 1, \tag{5.49}$$

an 1D CE/SE Euler solver can be used to obtain accurate shock tube solutions with the maximal *CFL* number in each numerical simulation ranging from 0.88 to 0.022.

(b) In a numerical simulation involving a nonuniform mesh, the local *CFL* number may vary sharply across the computational domain. For this case, the local values of ϵ, β, and α may be adjusted such that no excessive local numerical dissipation occurs in the computational domain.

6. NUMERICAL RESULTS

The accuracy of the 2D a and a-ϵ schemes were evaluated in [12] using a translating Gaussian hill model problem. Also, the accuracy of the 2D Euler solvers described in

Section 5 was evaluated in [8, 10, 20, 25] by comparing the computed results with exact or experimental results for numerous flow problems involving shocks, contact discontinuities, vortices, acoustic waves, and their interactions.

To give the reader a clear idea about the accuracy and robustness of the CE/SE method in general, and yet to not be burdensome with overly extensive numerical results, in this section we shall focus on the accuracy evaluation of the simplest 2D Euler scheme, i.e., that defined by Eqs. (EI-3.51) and (5.48). For reasons that will become clear to the reader shortly, we begin with a discussion of the concept of dual space-time meshes.

6.1. *Concept of Dual Space-Time Meshes*

Recall that the mesh point set Ω is defined in Section 3 such that $(j, k, n \pm 1/2) \notin \Omega$ if $(j, k, n) \in \Omega$. Let Ω' be defined such that $(j, k, n) \in \Omega'$ if and only if $(j, k, n \pm 1/2) \in \Omega$. As an example, consider Fig. 5a. Points A, C, E, and G' belong to Ω while points A', C', E', and G belong to Ω'. Obviously any of the 2D schemes described in Sections 3–5, e.g., the 2D *a* scheme, can also be constructed using the mesh points $(j, k, n) \in \Omega'$. As a matter of fact, one can even combine two independent 2D *a* schemes, one constructed using the mesh points $\in \Omega$ and the other using the mesh points $\in \Omega'$, into a "single" scheme referred to as the 2D dual *a* scheme. A mesh that contains all the mesh points belonging to either Ω or Ω' is referred to as a dual space-time mesh. Note that a CE of a mesh point $\in \Omega$ may coincide with a CE of another mesh point $\in \Omega'$.

Note that Ω_1 (Ω_2) was defined in Section 3 so that a mesh point $(j, k, n) \in \Omega_1$ (Ω_2) if and only if $(j, k, n) \in \Omega$ and n is a half-integer (a whole integer). Similarly, we define Ω'_1 (Ω'_2) so that a mesh point $(j, k, n) \in \Omega'_1$ (Ω'_2) if and only if $(j, k, n) \in \Omega'$ and n is a half-integer (a whole integer).

6.2. *Initial/Boundary Conditions*

The steady-state oblique shock problem suggested by Yee and others [32], one of the test problems to be considered later, will be used as the prototypical case in the following discussion.

The computational domain and the shock locations ($\overline{AE}$ and $\overline{EF}$) are depicted in Fig. 14. The lower boundary is a solid wall. Assuming $\gamma = 1.4$, then the exact Euler solutions to regions ABE, $AEFD$, and ECF are

$$u = 2.9, \quad v = 0., \quad \rho = 1.0, \quad p = 1.0/1.4 \quad \text{(region } ABE\text{)}, \tag{6.1}$$

$$u = 2.6193, \quad v = -0.50632, \quad \rho = 1.7000, \quad p = 1.5282 \quad \text{(region } AEFD\text{)}, \tag{6.2}$$

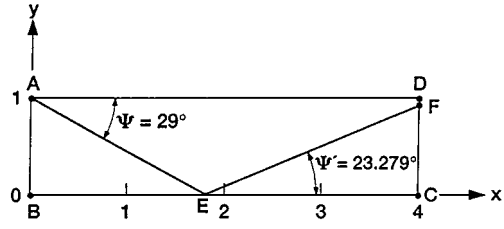

FIG. 14. The computation domain and the shock locations of a steady-state oblique shock problem.

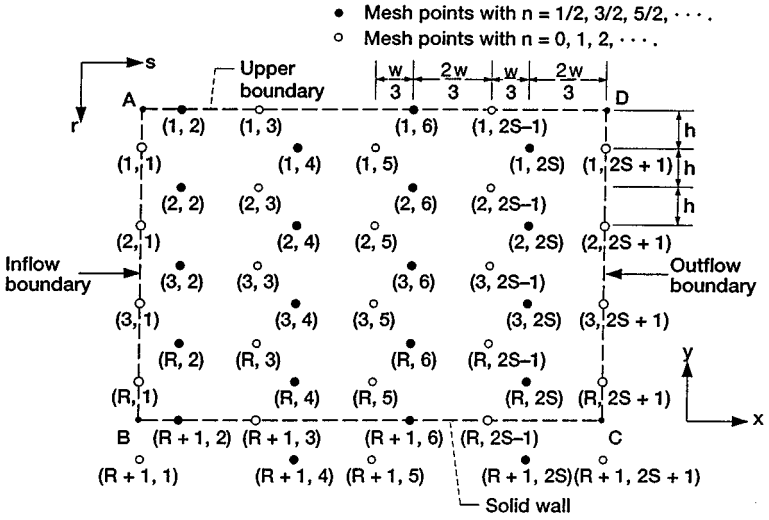

FIG. 15. The spatial locations and the mesh indices (r, s) of mesh points used in a steady-state oblique shock problem $(R = S = 4)$.

and

$$u = 2.4015, \quad v = 0., \quad \rho = 2.6872, \quad p = 2.9340 \quad (\text{region } ECF), \tag{6.3}$$

respectively.

The mesh used in this test problem is depicted in Fig. 15. Again a mesh point $(j, k, n) \in \Omega_1$ (Ω_2) is marked by a solid (hollow) circle. The mesh is a special case $(b = 0)$ of that depicted in Figs. 6–8. Note that only the mesh points $\in \Omega_2$ are present at the inflow and outflow boundaries. Moreover, a mesh point and the corresponding marching variable will be identified by the time-level number n and two new mesh indices r and s which are given in Fig. 15 as a pair of integers enclosed in parentheses. Note that, for the mesh points $\in \Omega_1$, $r = 1, 2, 3, \ldots, R, R+1$ and $s = 2, 4, 6, \ldots, 2S$. On the other hand, for the mesh points $\in \Omega_2$, $r = 1, 2, 3, \ldots, R, R+1$ and $s = 1, 3, 5, \ldots, 2S-1, 2S+1$.

With the above preliminaries, the initial and boundary conditions can now be specified. At all mesh points $(r, s, 0)$, it is assumed that (i) u_m, $m = 1, 2, 3, 4$ are evaluated using Eq. (6.1), and (ii)

$$u^+_{m\zeta} = u^+_{m\eta} = 0, \quad m = 1, 2, 3, 4. \tag{6.4}$$

Furthermore, for $n = 1, 2, 3, \ldots$, the above conditions (i) and (ii) are applied at all mesh points at the inflow boundary $\overline{AB}$ (see Fig. 15).

At the upper boundary $\overline{AD}$, for all $n = 1/2, 1, 3/2, 2, \ldots$, (i) u_m are evaluated using Eq. (6.2), and (ii) $u^+_{m\zeta}$ and $u^+_{m\eta}$ are evaluated using Eq. (6.4).

The solid-wall boundary conditions at $\overline{BC}$ will be constructed by assuming that, at any time t, the flow fields below and above $\overline{BC}$ are the mirror images of each other. By using the definitions of u_m given in Eq. (5.1) and the fact that $y = 0$ at any point on $\overline{BC}$, it can be shown that the last assumption implies that

$$u_m(x, -y, t) = u_m(x, y, t), \quad m = 1, 2, 4, \quad \text{and} \quad u_3(x, -y, t) = -u_3(x, y, t) \tag{6.5}$$

$$\frac{\partial u_m}{\partial x}(x,-y,t)=\frac{\partial u_m}{\partial x}(x,y,t)\quad\text{and}\quad\frac{\partial u_m}{\partial y}(x,-y,t)=-\frac{\partial u_m}{\partial y}(x,y,t),\quad m=1,2,4 \tag{6.6}$$

and

$$\frac{\partial u_3}{\partial x}(x,-y,t)=-\frac{\partial u_3}{\partial x}(x,y,t)\quad\text{and}\quad\frac{\partial u_3}{\partial y}(x,-y,t)=\frac{\partial u_3}{\partial y}(x,y,t). \tag{6.7}$$

The numerical boundary conditions corresponding to Eqs. (6.5)–(6.7) are

$$(u_m)^n_{R+1,s}=(u_m)^n_{R,s},\quad m=1,2,4,\quad\text{and}\quad(u_3)^n_{R+1,s}=-(u_3)^n_{R,s}, \tag{6.8}$$

$$(u_{mx})^n_{R+1,s}=(u_{mx})^n_{R,s}\quad\text{and}\quad(u_{my})^n_{R+1,s}=-(u_{my})^n_{R,s},\quad m=1,2,4, \tag{6.9}$$

and

$$(u_{3x})^n_{R+1,s}=-(u_{3x})^n_{R,s},\quad\text{and}\quad(u_{3y})^n_{R+1,s}=(u_{3y})^n_{R,s}, \tag{6.10}$$

respectively. According to Fig. 15, the range of s in Eqs. (6.8)–(6.10) is dependent on the time level n. Let (i) $S'=S$ if S is even; and (ii) $S'=S-1$ if S is odd. Then (i) $s=4, 8, 12, \ldots, 2S'$ if $n=1/2, 3/2, \ldots$, and (ii) $s=1, 5, 9, \ldots, 2S'+1$ if $n=1, 2, \ldots$. Furthermore, by using Eq. (C.4) in [7] with $b=0$, it can be shown that Eqs. (6.9) and (6.10) are equivalent to

$$(u^+_{m\zeta})^n_{R+1,s}=(u^+_{m\eta})^n_{R,s}\quad\text{and}\quad(u^+_{m\eta})^n_{R+1,s}=(u^+_{m\zeta})^n_{R,s},\quad m=1,2,4 \tag{6.11}$$

and

$$(u^+_{3\zeta})^n_{R+1,s}=-(u^+_{3\eta})^n_{R,s},\quad\text{and}\quad(u^+_{3\eta})^n_{R+1,s}=-(u^+_{3\zeta})^n_{R,s}, \tag{6.12}$$

respectively. Equations (6.8), (6.11), and (6.12) are the boundary conditions at the lower wall (a solid wall).

At the outflow boundary $\overline{CD}$, for any $n=1, 2, 3, \ldots$, and $r=1, 2, 3, \ldots, R$, we assume that

$$(u_m)^n_{r,2S+1}=(u_m)^{n-1/2}_{r,2S},\quad m=1,2,3,4 \tag{6.13}$$

$$(u_{mx})^n_{r,2S+1}=0,\quad m=1,2,3,4 \tag{6.14}$$

and

$$(u_{my})^n_{r,2S+1}=(u_{my})^{n-1/2}_{r,2S},\quad m=1,2,3,4. \tag{6.15}$$

Note that, because $b=0$, Eqs. (6.14) and (6.15) are equivalent to

$$(u^+_{m\zeta})^n_{r,2S+1}=\frac{1}{2}(u^+_{m\zeta}-u^+_{m\eta})^{n-1/2}_{r,2S},\quad m=1,2,3,4 \tag{6.16}$$

and

$$(u^+_{m\eta})^n_{r,2S+1}=\frac{1}{2}(u^+_{m\eta}-u^+_{m\zeta})^{n-1/2}_{r,2S},\quad m=1,2,3,4. \tag{6.17}$$

Thus the marching variables at the outflow boundary can be determined using Eqs. (6.13), (6.16), and (6.17). Note that, according to the numerical results to be presented, the outflow boundary conditions are nonreflecting in nature.

With the aid of the above initial and boundary conditions, the marching variables at all mesh points (including those located at the bottom solid wall $\overline{BC}$) can be determined by using the scheme defined by Eqs. (EI-3.51) and (5.48).

In the oblique shock problem described above, only a horizontal solid wall is present. In other 2D test problems to be described later, both horizontal and vertical solid walls may be present. As will be shown immediately, imposing the solid-wall boundary conditions at a vertical wall over a uniform mesh similar to that depicted in Fig. 15 is slightly more complicated than that at a horizontal wall.

Consider the mesh depicted in Fig. 16a. Let $\overline{BC}$ and $\overline{CD}$ be solid walls. Note that, given any exterior mesh point $(R+1, s, n)$ that lies immediately below $\overline{BC}$, one can find an

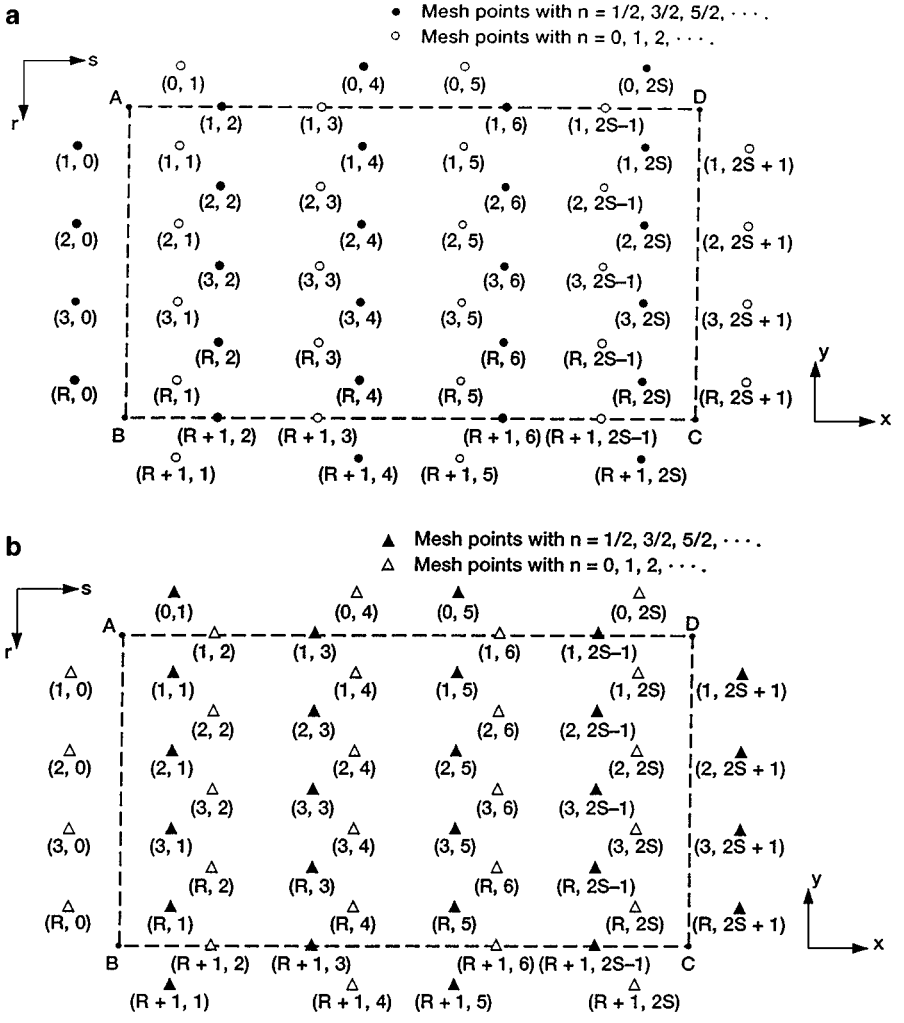

FIG. 16. The spatial locations and the mesh indices (r, s) of mesh points used in a problem with both horizontal and vertical walls. (a) Mesh points $\in \Omega$. (b) Mesh points $\in \Omega'$.

interior mesh point that lies at the same time level and also is the mirror image (relative to $\overline{BC}$) of the exterior mesh point. As a result, the solid-wall boundary conditions Eqs. (6.8)–(6.10) can be imposed. Contrarily, given any exterior mesh point $(r, 2S+1, n)$, $n=0, 1, 2, \ldots$ that lies immediately to the right of $\overline{CD}$, one cannot find an interior mesh point that lies at the same time level and is the mirror image (relative to $\overline{CD}$) of the exterior mesh point. As a result, the mirror image conditions for the vertical wall $\overline{CD}$, i.e.,

$$(u_m)^n_{r,2S+1} = (u_m)^n_{r,2S}, \quad m = 1, 3, 4, \quad \text{and} \quad (u_2)^n_{r,2S+1} = -(u_2)^n_{r,2S} \tag{6.18}$$

$$(u_{mx})^n_{r,2S+1} = -(u_{mx})^n_{r,2S} \quad \text{and} \quad (u_{my})^n_{r,2S+1} = (u_{my})^n_{r,2S}, \quad m = 1, 3, 4 \tag{6.19}$$

and

$$(u_{2x})^n_{r,2S+1} = (u_{2x})^n_{r,2S}, \quad \text{and} \quad (u_{2y})^n_{r,2S+1} = -(u_{2y})^n_{r,2S} \tag{6.20}$$

cannot be used directly as the solid-wall boundary conditions.

Two approaches can be used to overcome the above difficulty. In the first and more restrictive approach, the following approximate forms of Eqs. (6.18)–(6.20) are used as the solid-wall boundary conditions:

$$(u_m)^n_{r,2S+1} = (u'_m)^n_{r,2S}, \quad m = 1, 3, 4, \quad \text{and} \quad (u_2)^n_{r,2S+1} = -(u'_2)^n_{r,2S} \tag{6.21}$$

$$(u_{mx})^n_{r,2S+1} = -(u_{mx})^{n-1/2}_{r,2S} \quad \text{and} \quad (u_{my})^n_{r,2S+1} = (u_{my})^{n-1/2}_{r,2S}, \quad m = 1, 3, 4 \tag{6.22}$$

and

$$(u_{2x})^n_{r,2S+1} = (u_{2x})^{n-1/2}_{r,2S}, \quad \text{and} \quad (u_{2y})^n_{r,2S+1} = -(u_{2y})^{n-1/2}_{r,2S}. \tag{6.23}$$

Here $(u'_m)^n_{r,2S}$, $m=1, 2, 3, 4$, are evaluated using the known marching variables at the mesh point $(r, 2S, n-1/2)$ with the aid of the first-order Taylor's expansion.

In the second and generally more accurate and preferable approach, the present marching procedure is applied over a dual mesh, i.e., the combination of two staggered space-time meshes depicted in Figs. 16a and 16b. As shown in Fig. 16b, a mesh point $\in \Omega'$ is also identified by two spatial indices r and s and the time-level number n. Furthermore, a mesh point $\in \Omega'_1$ (Ω'_2) is marked by a solid (hollow) triangle.

Note that: (i) for $n=0, 1, 2, \ldots$, $(r, 2S+1, n)$ is a mesh point $\in \Omega$ while $(r, 2S, n)$ is a mesh point $\in \Omega'$, (ii) for $n=1/2, 3/2, 5/2, \ldots$, $(r, 2S+1, n)$ is a mesh point $\in \Omega'$ while $(r, 2S, n)$ is a mesh point $\in \Omega$, and (iii) for any $n=0, 1/2, 1, 3/2, \ldots$, the mesh points $(r, 2S+1, n)$ and $(r, 2S, n)$ lie at the same time level and, relative to $\overline{CD}$, are mirror images of each other. As a result, at any time level, the solid-wall boundary conditions at $\overline{CD}$ can be imposed using Eqs. (6.18)–(6.20). Note that, as a result of these boundary conditions, the marching variables associated with the mesh points $\in \Omega$ are now coupled with those associated with the mesh points $\in \Omega'$. Also note that the Eqs. (6.19), (6.20), (6.22), and (6.23) can easily be converted to the versions associated with the (ζ, η) coordinates by using Eq. (C.4) of [7] with $b=0$.

Imposing the conditions Eqs. (6.18)–(6.20) directly requires the use of a dual mesh. As a result, it has the disadvantage of doubling computational cost. However, the extra cost no longer becomes an issue in a case in which its use is mandatory, e.g., a numerical simulation involving unstructured meshes [13, 14].

6.3. *Four Test Problems*

In this part, one steady-state problem and three time-dependent problems are solved using the scheme defined by Eqs. (EI-3.51) and (5.48). A steady-state solution is obtained as the converged solution of the time-marching procedure. In all numerical simulations, $\alpha = 2$ is assumed throughout the entire computational domain. Because α is the only adjustable parameter in the present scheme, the same numerical treatment is applied at all interior mesh points for all four test problems. Also note that, without exception, the numerical results to be shown are those of the entire computational domain; i.e., no buffer-zone techniques are used.

To pave the way for the following presentation, a further discussion of the space-time mesh depicted in Fig. 15 is in order. According to Fig. 15, at each time level $n = 0, 1, 2, \ldots$, there are $S + 1$ staggered columns of mesh points (marked by hollow circles) with each column containing $R + 1$ mesh points. Thus, there are $(S + 1) \times (R + 1)$ mesh points at each of these time levels. Furthermore, because two neighboring columns are separated by a distance w while two neighboring mesh points in any column are separated by a distance $2h$, we have $S = W/w$ and $R = H/(2h)$, where W and H are the width and height of the computational domain, respectively. If the first, the third, the fifth, ... columns were moved upward a distance h, then the mesh points marked by hollow circles would form a regular Cartesian spatial mesh with S and R mesh intervals in the x- and y-directions, respectively. As a result, the mesh formed by the mesh points marked by hollow circles will be referred to as a $S \times R$ mesh.

Similarly, at each time level $n = 1/2, 3/2, \ldots$, there are S staggered columns of mesh points (marked by solid circles) with each column containing $R + 1$ mesh points. Again two neighboring columns are separated by a distance w and two neighboring mesh points in any column are separated by a distance $2h$. In this paper, the mesh formed by these mesh points will also be referred to as a $S \times R$ mesh. In general, regardless of how its columns of mesh points are positioned, a spatial mesh covering a rectangular computational domain of width W and height H will be referred to as a $(W/w) \times (H/(2h))$ mesh if two neighboring columns of mesh points are separated by a distance w and two neighboring mesh points in any column are separated by a distance $2h$.

For the dual mesh referred to earlier, there are two sets of mesh points at one time level. If each set forms a $(W/w) \times (H/(2h))$ mesh, then the dual mesh will be referred to as a dual $(W/w) \times (H/(2h))$ mesh.

From the above analysis and the fact that it requires two marching steps to advance by a time period Δt in the CE/SE method, the total number of space-time mesh points involved in a 2D CE/SE simulation is approximately equal to $(2T/\Delta t) \times S \times R$, i.e., about twice that of a 2D single-step regular-mesh simulation if each simulation uses a $S \times R$ mesh and both have the same values of Δt and total simulation time T. Note that, in the special case that a dual $S \times R$ mesh is used, the total number of mesh points involved in a CE/SE simulation is approximately equal to $(4T/\Delta t) \times S \times R$.

To give the reader some idea about the computational efficiency of the present scheme, note that, for a 300×120 mesh, the CPU time on a Cray C90 required to execute 180 marching steps ($T = 180 \times (\Delta t/2)$) is only 14 s, i.e., about 2.16 μs per mesh point per marching step.

6.3.1. Oblique shock problem. The computational domain, mesh structure, and initial/boundary conditions used in the current simulations of this problem were described in

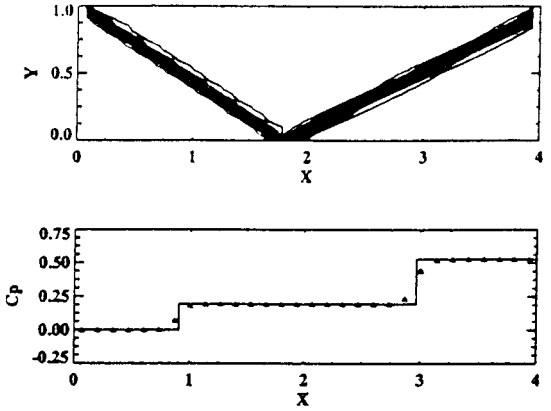

FIG. 17. Pressure contours and pressure coefficient at $y = 0.5$ of the oblique shock problem (60×20 mesh).

Section 6.2. A numerical simulation is carried out using a 60×20 mesh with $\Delta t = 0.01$. The resulting steady-state density contours and the pressure coefficient C_p $(=2(p/p_\infty - 1)/(\gamma M_\infty^2)$ with $M_\infty = 2.9$ and $p_\infty = 1.0/1.4$ being the inflow Mach number and pressure, respectively) at $y = 0.5$ are plotted in Fig. 17, where the solid line represents the exact solution. The improvement in shock resolution by using a finer 120×40 mesh can be seen in Fig. 18. No numerical oscillations are detected near either the incident or the reflected shocks, and the computed C_p agrees very well with the exact solution. Moreover, the reflected shock is as crisp as the incident shock.

6.3.2. 2D supersonic flow past a step. Consider the supersonic channel flow of $M_s = 3.0$ past a step depicted in Fig. 19. This benchmark problem was used to test Harten's TVD ULT1C scheme [33], Giannakouros and Karniadakis's spectral element-FCT method [34], and Van Leer's ultimate conservative difference scheme [35]. It was also used by Woodward and Colella [36] to compare the accuracy of different numerical methods in handling a shock discontinuity.

Note that the upper corner of the step is the center of a rarefaction fan and hence is a singular point of the flow. According to Woodward and Colella [36], unless special numerical treatments are applied near the corner of the step, the computed solutions would be seriously

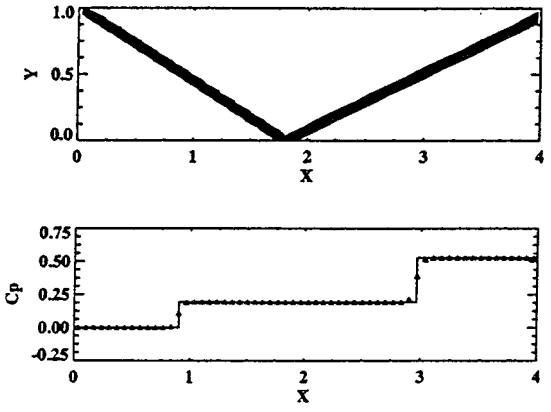

FIG. 18. Pressure contours and pressure coefficient at $y = 0.5$ of the oblique shock problem (120×40 mesh).

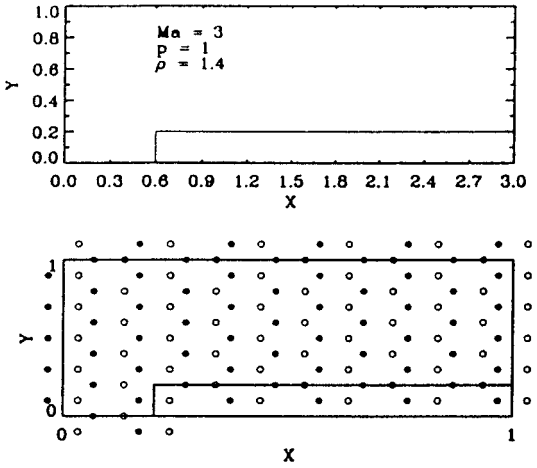

FIG. 19. Geometry and grid distribution of the 2D supersonic flow past a step problem.

affected by large numerical errors generated in the neighborhood of this singular point. It will be shown immediately that satisfactory numerical solutions can be obtained by the present scheme without employing special treatments at the upper corner of the step.

The mesh used in the current simulation is also depicted in Fig. 19. Note that no mesh point is placed at the singular point at the upper corner of the step. The initial conditions are set to be the free stream conditions. Furthermore, the constant free stream conditions are imposed at the inlet while the nonreflecting boundary conditions Eqs. (6.13), (6.16), and (6.17) are imposed at the exit. In addition, the reflecting (solid-wall) boundary conditions are imposed at all other boundaries.

To show the improvement in flow solutions with decreased mesh spacing, the density contours of the solutions obtained by the present solver with 60×20, 120×40, and 240×80 meshes are shown respectively in Fig. 20. Note that the values of Δt used in the above computations are identical to those used in [36], i.e., 0.0075, 0.005, and 0.0025, repectively ($CFL \doteq 0.8$). From Fig. 20, it is seen that the Mach stem, triple point, slip surface, expansion fan at the corner, and the interaction between the reflected shock and the rarefaction waves are accurately simulated in the present solutions. Note that an alternate simulation in which the dual-mesh reflecting boundary conditions Eqs. (6.18)–(6.20) are imposed at the vertical step wall yields almost identical results.

6.3.3. Shock reflection from a dust layer. Here, a practical problem of shock reflection from a dust layer is studied. Following the wedge model described in [37], we consider a plane shock moving to the right with Mach number $M_s = 1.41$ toward a wedge whose surface is inclined at angle θ_w, as shown in Fig. 21. Square protuberances of size $L/2$ are placed at equal distances L apart on the surface to simulate dust particles. The common origin of the two coordinate systems (x, y) and (x', y') is situated at the tip of the wedge, with the x'- and y'-axes being parallel and normal to the wedge surface, respectively.

As depicted in Fig. 22, the computational domain ($-0.5 \le x'/L \le 7.0$ and $0 \le y'/L \le 4$) contains seven protuberances. The front of the incident shock thus makes an angle θ_w with the y'-axis. At $t = 0$, the computational domain is divided into two flow regions by the shock front that intersects the x'-axis at $x'/L = -0.4$. Standard stationary atmospheric conditions are assumed in the region to the right of the shock front, while constant fluid conditions with

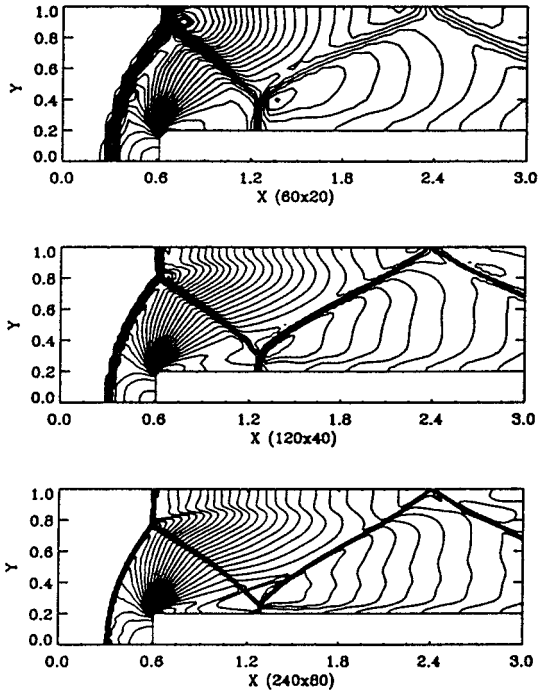

FIG. 20. Density contours of the 2D supersonic flow past a step problem generated using 60×20, 120×40, and 240×80 meshes.

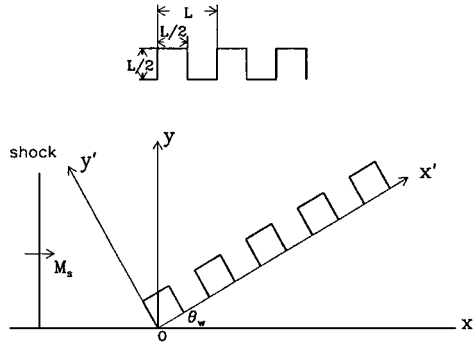

FIG. 21. Shock moving past a wedge with a dust layer.

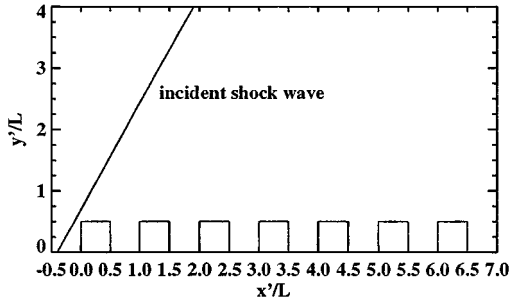

FIG. 22. The computational domain of the dust layer problem.

$M_s = 1.41$ are assumed in the other region. Reflecting boundary conditions are imposed at all solid walls, while nonreflecting boundary conditions are implemented both at the inlet and outlet and on the part of x'-axis with $-0.5 \le x'/L \le 0$, through which waves can move freely. On the upper boundary ($y'/L = 4$), where the reflected waves have not reached before the end of all simulations, numerical values are assigned ahead of and behind the plane shock according to the exact solution. Computations were carried out for $\theta_w = 20^\circ$, 30°, and 40°, respectively, using a 300×180 mesh with $\Delta t = 0.01$, where t is made dimensionless using L as the reference length and the speed of sound in the undisturbed region as the reference speed.

In order to show a clear comparison between the experimental and computed results, the CE/SE solutions are plotted in the (x, y)-coordinates through a coordinate transformation. First, to show the unsteady evolution of wave patterns resulting from the reflection of shock waves over the dusty wedge, computed density contours at four different time levels for $\theta_w = 30^\circ$ are plotted in Fig. 23. The effect of varying wedge angle on wave pattern can be observed in the density contour plots shown in Fig. 24 for $\theta_w = 20^\circ$ at $t = 3.8$ and in Fig. 25 for $\theta_w = 40^\circ$ at $t = 3.0$, when the incident shock wave is standing at the upper right corner of the sixth protuberance. The Schlieren photographs taken from [37] are reproduced in Figs. 26–28 to show representative wave patterns for the cases $\theta_w = 20^\circ$, 30°, and 40° at different instants. In these photographs, (i) Model B and Model D represent the laboratory models with $L = 8$ and 2 mm, respectively, and (ii) T_1 denotes the triple point generated by the reflection of shock waves from the first protuberance. The location of T_1 in the x-direction is indicated by the numerical value of x/L in each figure. It is seen that, as the incident shock wave moves forward, a compression wave is reflected from each protuberance and an expansion wave is generated from its back. Gradually, the individual compression waves accumulate to form an envelope C_e and a stronger compression wave C'_e (see Fig. 27). For the cases with $\theta_w = 20^\circ$ and $\theta_w = 30^\circ$, the developments of wave patterns are almost the same, while for $\theta_w = 40^\circ$, a kink point K appears as shown in Fig. 28. A comparison between experimental and numerical results indicates that the photographed wave patterns are correctly captured in the CE/SE solutions. The close resemblance between Figs. 24 and 26 and that between Figs. 23d and 27 in terms of both wave and vortex structures are clearly recognizable.

6.3.4. Implosion/explosion of polygonal shock waves in a box. The problem concerning the implosion/explosion of a polygonal shock wave in a square box studied in [38] is investigated here. Not only the early stage of the implosion/explosion process, but also its later development, which was not studied in [38], are simulated here.

All simulations are carried out using (i) a dual 240×240 mesh covering a square box ($-2 \le x, y \le 2$), and (ii) a *CFL* number $= 0.9$. The reflecting boundary conditions are imposed at the four sides of the square box with the understanding that the more accurate dual-mesh reflecting boundary conditions Eqs. (6.18)–(6.20) are used at the vertical walls.

The initial shock wave configuration is a regular polygon. It is assumed that (i) the polygon shares with the square box the same geometric center (located at $(0, 0)$), (ii) one of the vertices of the polygon is located at $(0, 0.8 \times \sqrt{3})$, and (iii) there is a low pressure region inside the polygon with a pressure ratio of 10 across the shock. Note that, as a result of (i) and (ii), the vertices of the polygon are points on the circumference of the circle that has a radius $= 0.8 \times \sqrt{3}$ and is centered at $(0, 0)$.

As the first step, the early flow field is studied for three cases in which the initial shock wave configurations are an equilateral triangle, a square, and a regular pentagon,

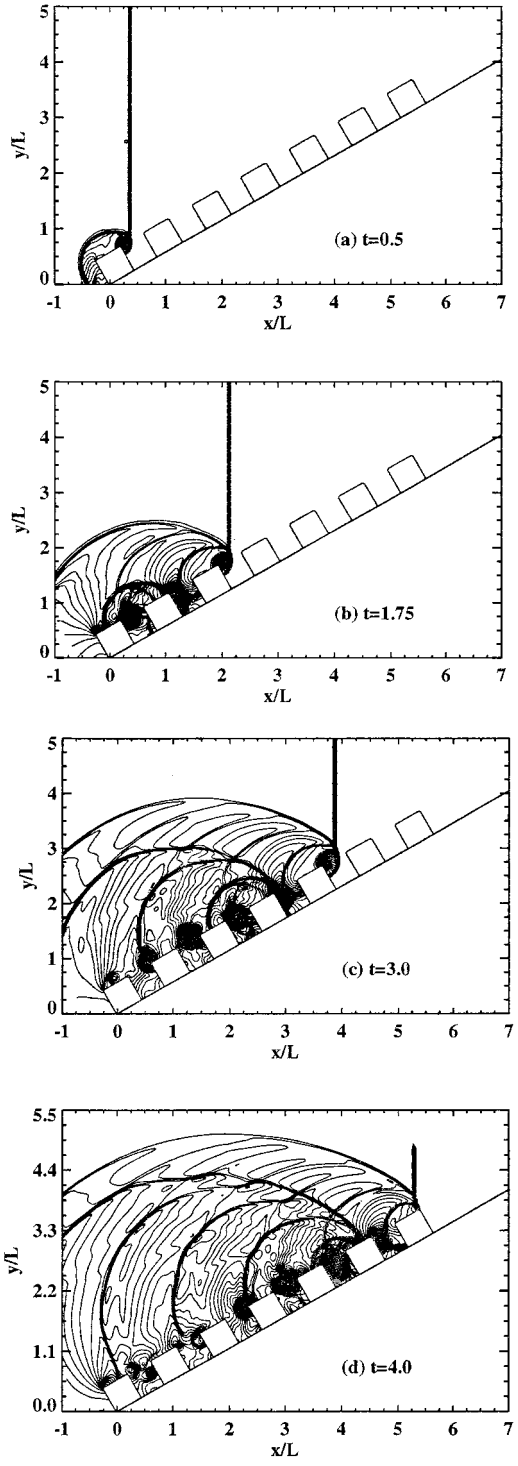

FIG. 23. Density contours for the dust layer problem ($\theta_w = 30^\circ$) at four different time levels. (a) $t = 0.5$, (b) $t = 1.75$, (c) $t = 3$, (d) $t = 4$.

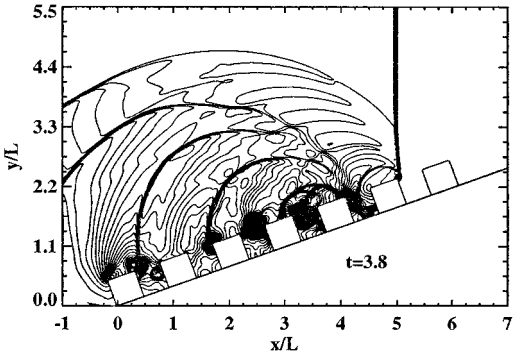

FIG. 24. Density contours at $t = 3.8$ for the dust layer problem ($\theta_w = 20^\circ$).

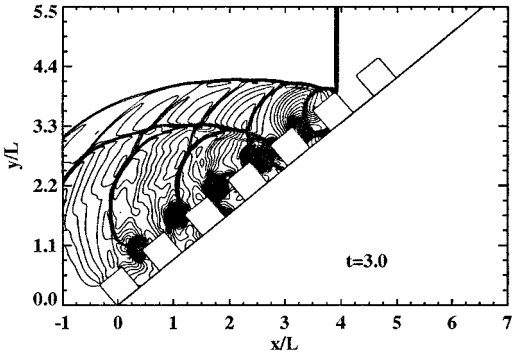

FIG. 25. Density contours at $t = 3.0$ for the dust layer problem ($\theta_w = 40^\circ$).

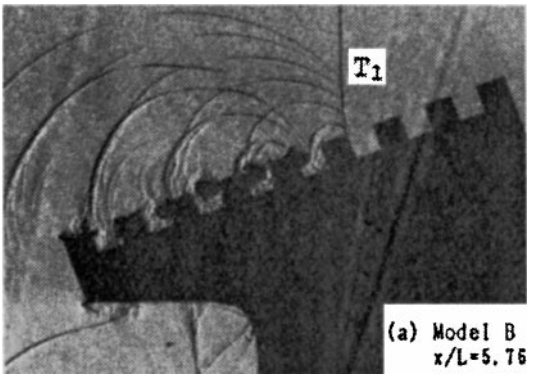

FIG. 26. A Schlieren photography for $\theta_w = 20^\circ$.

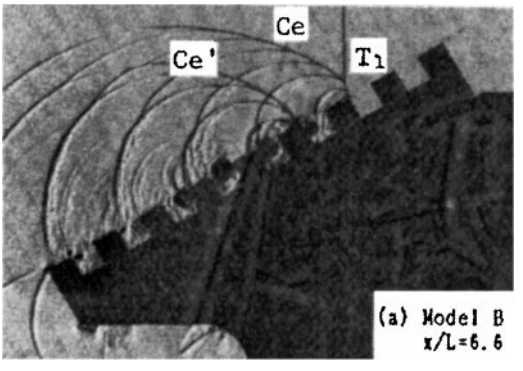

FIG. 27. A Schlieren photography for $\theta_w = 30^\circ$.

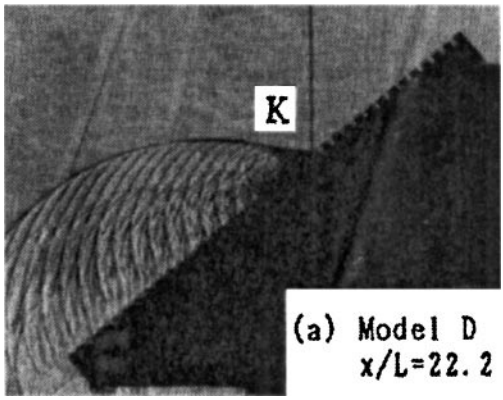

FIG. 28. A Schlieren photography for $\theta_w = 40^\circ$.

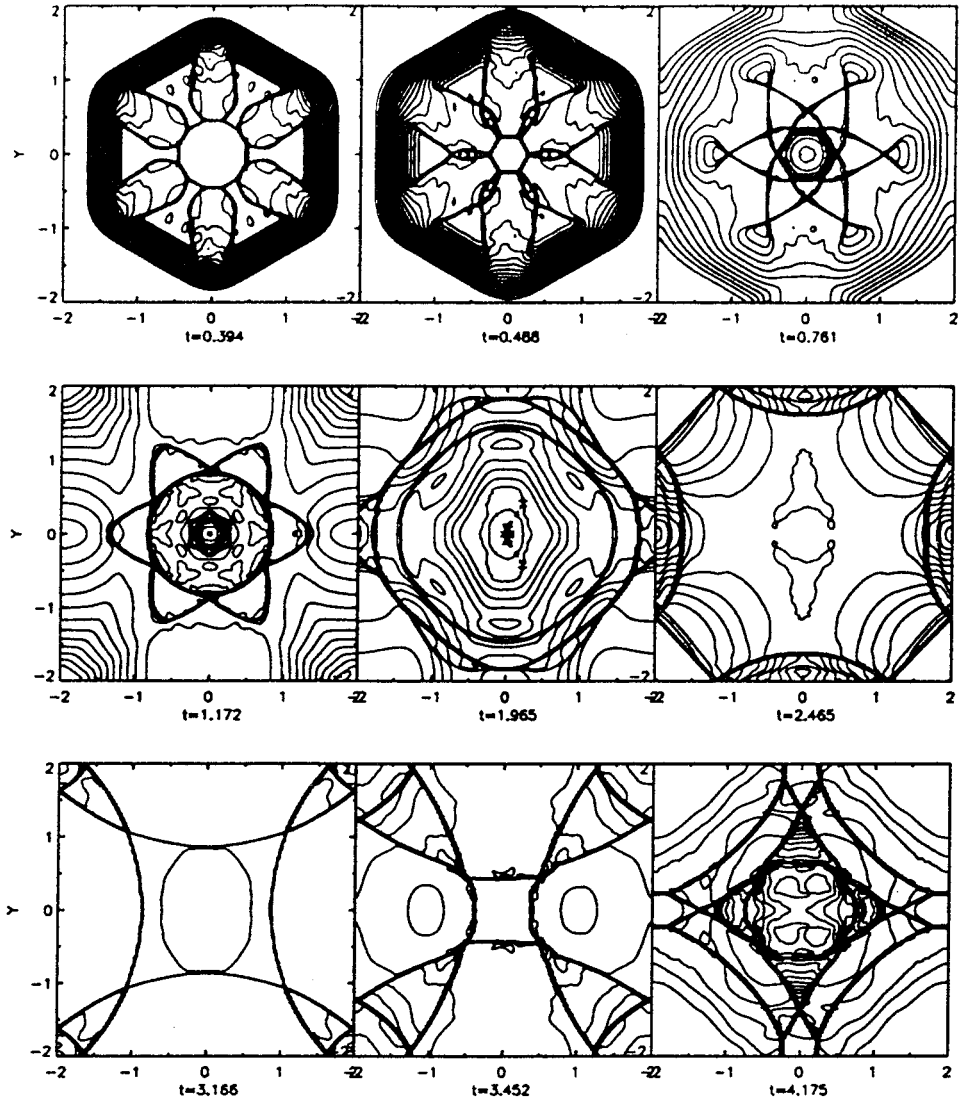

FIG. 29. Pressure contours for implosion/explosion of a hexagonal shock in a square box.

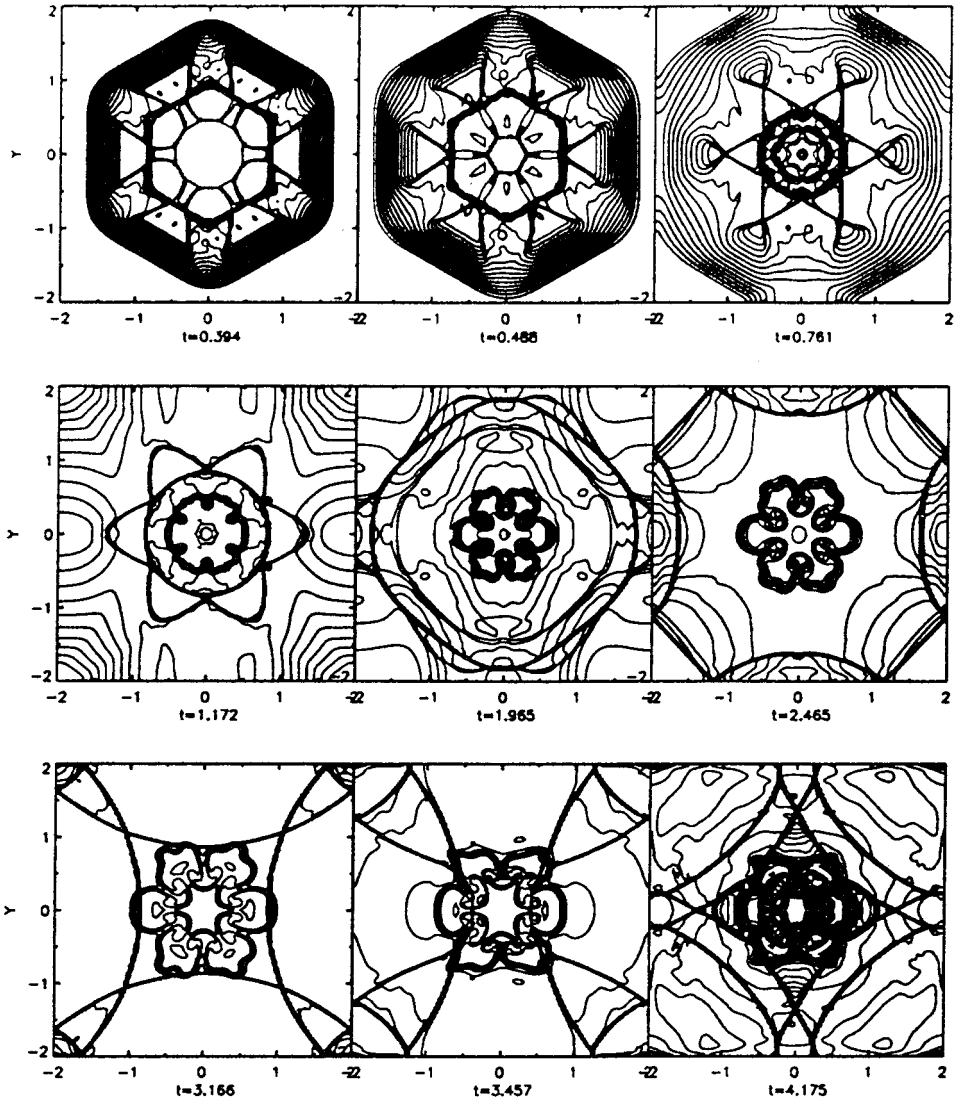

FIG. 30. Density contours for implosion/explosion of a hexagonal shock in a square box.

respectively. The computed pressure and density contour plots at different time levels are shown in Figs. 38 and 39 of [8], respectively. According to these figures, wave patterns similar to those shown in Figs. 1–5 of [38], obtained using a TVD method on a 359×359 mesh, are also observed in the CE/SE solutions, displaying detailed features such as Mach stems and polygon-shaped flow discontinuities.

As the second step, the implosion/explosion of a hexagonal shock wave is simulated until the second implosion of the shock wave is observed in the box. More complex flow phenomena can be seen in the pressure and density contour plots of Figs. 29 and 30, including the reflections of shock waves, shock–shock interaction, and shock–contact surface interaction. It is interesting to note that the shocks and contact discontinuities are still relatively crisp after multiple reflections of shock waves from solid walls.

7. CONCLUSIONS AND RECENT DEVELOPMENTS

The space-time CE/SE method was conceived from nontraditional basic beliefs and designed to avoid the limitations of the traditional methods. It was built from ground zero with a foundation that is solid in physics and yet mathematically simple enough that one can build from it a coherent, robust, efficient, and accurate CFD numerical framework. In this paper, we begin with a clear and thorough discussion of the above motivating ideas (Section 1). It is then followed by a rigorous exposition of the 2D theoretical development (Sections 2–5).

To evaluate the accuracy and robustness of the 2D Euler CE/SE schemes, the simplest among them, i.e., that defined by Eqs. (EI-3.51) and (5.48), was evaluated in Section 6. It was shown that this scheme can accurately resolve shock and contact discontinuities consistently. Furthermore, it was shown that the scheme is genuinely robust, i.e., it is compatible with the simplest nonreflecting boundary conditions, and its accuracy is achieved without resorting to special treatments for each individual case. Moreover, because it is logically simple and totally explicit, the scheme is also highly computationally efficient. As a result, generally it is recommeded that the simplest scheme be used except in the difficult case discussed in Section 5.5.

Note that other CE/SE schemes described in this paper have also been shown to be accurate solvers for other applications [8, 11, 20, 21, 25].

The paper is concluded with a discussion of recent CE/SE related developments:

(a) By using the marching variables that are tied to the Cartesian coordinates (x, y), the concepts described in this paper can be easily extended to construct CE/SE Euler solvers for irregular triangular meshes [12] or even unstructured triangular meshes [13, 18]. The accuracy of these solvers has been validated by comparing the numerical results of numerous test problems with the experimental results. Note that it is shown in [18] that, without using any preconditioning technique, the 2D CE/SE method can generate accurate numerical solutions for flows with speeds ranging from Mach number $= 0.00288$ to 10.

(b) By using tetrahedrons as the basic building blocks of the spatial meshes, a 3D CE/SE Euler solver compatible with both structured and unstructured meshes has recently been constructed and described in detail in [14]. The accuracy of this 3D solver and that of another similar 3D Euler solver [18] have been validated using the following test problems: (i) the implosion and explosion of a spherical shock wave in a cubical box, (ii) a supersonic flow over a 3D ramp, and (iii) a hypersonic flow ($M_\infty = 10$) over a 3D half sphere.

(c) To be compatible with the simplest unstructured meshes, most of the multidimensional CE/SE solvers were developed using triangles and tetrahedrons, respectively, as the basic building blocks of 2D and 3D spatial meshes. However, it is shown in [22–25] that the 2D and 3D nonsplitting CE/SE Euler solvers can also be constructed using rectangular meshes. The accuracy of these new solvers is comparable with that of other CE/SE solvers.

(d) Several 2D and 3D CE/SE Navier–Stokes solvers using rectangular, triangular, and tetrahedral meshes have also been constructed recently. In [23], two test problems, i.e., (i) shock/boundary layer interaction with $M_\infty = 2$ and (ii) natural convection flows in a square box, are used to validate the accuracy of a 2D CE/SE Navier–Stokes solver in solving both high-speed and low-speed flows.

(e) Both 1D and 2D solvers for flows involving chemical reactions have recently been developed by Yu *et al.* [15, 16].

(f) An advanced fluid dynamic code for the simulation of 1D unsteady flows in engine ducts, named GASDYN, has been developed by Onorati *et al.* [17]. An extended 1D CE/SE scheme capable of dealing with the propagation of chemical species is adopted in the code. It is concluded in [17] that "a comparison of the MacCormack method plus FCT or TVD algorithms with the CE–SE method has pointed out the superiority of the latter scheme in the propagation of contact discontinuities."

REFERENCES

1. S. C. Chang and W. M. To, *A New Numerical Framework for Solving Conservation Laws—The Method of Space-Time Conservation Element and Solution Element*, NASA TM 104495, August 1991.
2. S. C. Chang, The method of space-time conservation element and solution element—A new approach for solving the Navier–Stokes and Euler equations, *J. Comput. Phys.* **119**, 295 (1995).
3. P. Batten, M. A. Leschziner, and U. C. Goldberg, Average-state Jacobians and implicit methods for compressible viscous and turbulent flows, *J. Comput. Phys.* **137**, 38 (1997).
4. T. Molls and F. Molls, Space-time conservation method applied to Saint Venant equations, *J. Hydraulic Engrg.* **124**(5), 501 (1998).
5. C. Zoppou and S. Roberts, Space-time conservation method applied to Saint Venant equations: A discussion, *J. Hydraulic Engrg*. **125**(8), 891 (1999).
6. S. C. Chang, S. T. Yu, A. Himansu, X. Y. Wang, C. Y. Chow, and C. Y. Loh, The method of space-time conservation element and solution element—A new paradigm for numerical solution of conservation laws, in *Computational Fluid Dynamics Review* edited by M. M. Hafez and K. Oshima (World Scientific, Singapore, 1998), Vol. 1.
7. S. C. Chang, X. Y. Wang, and C. Y. Chow, *The Space-Time Conservation Element and Solution Element Method—A New High-Resolution and Genuinely Multidimensional Paradigm for Solving Conservation Laws. I. The Two-Dimensional Time Marching Schemes*, NASA TM 208843, December 1998.
8. X. Y. Wang, C. Y. Chow, and S. C. Chang, *The Space-Time Conservation Element and Solution Element Method—A New High-Resolution and Genuinely Multidimensional Paradigm for Solving Conservation Laws. II. Numerical Simulation of Shock Waves and Contact Discontinuities*, NASA TM 208844, December 1998.
9. S. C. Chang, On an origin of numerical diffusion: Violation of invariance under space-time inversion, in *Proceedings of the 23rd Modeling and Simulation Conference, April 30–May 1, 1992, Pittsburgh, PA*, edited by William G. Vogt and Marlin H. Mickle, Part 5, p. 2727. [Also published as NASA TM 105776.]
10. S. C. Chang, X. Y. Wang, and C. Y. Chow, *New Developments in the Method of Space-Time Conservation Element and Solution Element—Applications to Two-Dimensional Time-Marching Problems*, NASA TM 106758, December 1994.
11. X. Y. Wang, C. Y. Chow, and S. C. Chang, *Application of the Space-Time Conservation Element and Solution Element Method to Two-Dimensional Advection-Diffusion Problems*, NASA TM 106946, June 1995.
12. X. Y. Wang, *Computational Fluid Dynamics Based on the Method of Space-Time Conservation Element and Solution Element*, Ph.D. dissertation (Department of Aerospace Engineering Sciences, University of Colorado at Boulder, 1995).
13. X. Y. Wang and S. C. Chang, A 2D non-splitting unstructured triangular mesh Euler solver based on the space-time conservation element and solution element method, *Comput. Fluid Dynamics J.* **8**(2), 309 (1999).
14. X. Y. Wang and S. C. Chang, A 3D structured/unstructured Euler solver based on the space-time conservation element and solution element method, in *A Collection of Technical Papers, 14th AIAA CFD Conference, June 28–July 1, 1999, Norfolk, Virginia*, AIAA Paper 99-3278.
15. S. T. Yu and S. C. Chang, Applications of the space-time conservation element/solution element method to unsteady chemically reactive flows, in *A Collection of Technical Papers, 13th AIAA CFD Conference, June 29-July 2, 1997, Snowmass, Colorado*, AIAA Paper 97-2099.
16. S. T. Yu, S. C. Chang, P. Jorgenson, S. J. Park, and M. C. Lai, Treating stiff source terms in conservation laws by the space-time conservation element and solution element method, in *Proceedings of the 16th International Conference on Numerical Method in Fluid Dynamics, Arcachon, France, July 6–July 10, 1998*.

17. A. Onorati, G. Ferrari, and G. D'Errico, Fluid dynamics modeling of the gas flow with chemical specie transport through the exhaust manifold of a four cylinder SI engine, in *SAE Int. Congress & Exp*., Detroit, Michigan (March 1999) (Paper 1999-01-0557.)
18. N. S. Liu and K. H. Chen, *Flux: An Alternative Flow Solver for the National Combustion Code*, AIAA Paper 99-1079.
19. S. C. Chang, A. Himamsu, C. Y. Loh, X. Y. Wang, S. T. Yu, and P. Jorgenson, Robust and simple non-reflecting boundary conditions for the space-time conservation element and solution element method, in *A Collection of Technical Papers, 13th AIAA CFD Conference, June 29–July 2, 1997, Snowmass, Colorado*, AIAA Paper 97-2077.
20. C. Y. Loh, L. S. Hultgren, and S. C. Chang, *Computing Waves in Compressible Flow Using the Space-Time Conservation Element and Solution Element method*, AIAA Paper 98-0369.
21. C. Y. Loh, L. S. Hultgren, and S. C. Chang, *Vortex Dynamics Simulation in Aeroacoustics by the Space-Time Conservation Element and Solution Element Method*, AIAA Paper 99-0359.
22. Z. C. Zhang and S. T. Yu, *Shock Capturing without Riemann Solver—A Space-Time Method for Hyperbolic Conservation Laws*, AIAA Paper 99-0904.
23. Z. C. Zhang, S. T. Yu, S. C. Chang, A. Himansu, and P. Jorgenson, *A Modified Space-Time CE/SE Method for Solving Euler and Navier–Stokes Equations*, in *A Collection of Technical Papers, 14th AIAA CFD Conference, June 28–July 1, 1999, Norfolk, Virginia*, AIAA Paper 99-3277.
24. G. Cook, *High Accuracy Capture of Curved Shock Fronts Using the Method of Space-Time Conservation Element and Solution Element*, AIAA Paper 99-1008.
25. Other CE/SE references are posted on the web site: http://www.grc.nasa.gov/www/microbus.
26. D. Sidilkover, *A Genuinely Multidimensional Upwind Scheme and Efficient Multigrid Solver for the Compressible Euler Equations*, ICASE Report 94-84, ICASE, 1994.
27. G. A. Sod, A survey of several finite difference methods for systems of nonlinear hyperbolic conservation laws, *J. Comput. Phys.* **27**, 1 (1978).
28. C. Hirsch, *Numerical Computation of Internal and External Flows, Vol. 2: Computational Methods for Inviscid and Viscous Flows* (Wiley, New York, 1990).
29. J. Casper and M. H. Carpenter, Computational considerations for the simulation of shock-induced sound, *SIAM J. Sci. Comput.* **19**, 813 (1998).
30. D. A. Anderson, J. C. Tannehill, and R. H. Pletcher, *Computational Fluid Mechanics and Heat Transfer* (Hemisphere, New York, 1984).
31. R. Courant and D. Hilbert, *Methods of Mathematical Physics* (Interscience, New York, 1962), Vol. II.
32. H. C. Yee, R. F. Warming, and A. Harten, *Implicit Total Variation Diminishing (TVD) Schemes for Steady-State Calculations*, AIAA Paper 83-1902 (1983).
33. A. Harten, High resolution schemes for hyperbolic conservation laws, *J. Comput. Phys.* **49**, 357 (1983).
34. J. Giannakouros and G. E. Karniadakis, A spectral element-FCT method for the compressible Euler equations, *J. Comput. Phys.* **115**, 65 (1994).
35. B. van Leer, Toward the ultimate conservative difference scheme. V. A second-order sequel to Godunov's method, *J. Comput. Phys.* **32**, 101 (1979).
36. P. Woodward and P. Colella, The numerical simulation of two-dimensional fluid flow with strong shock, *J. Comput. Phys.* **54**, 115 (1984).
37. T. Suzuki, T. Adachi, and S. Kobayashi, An experimental analysis on shock reflection over the two-dimensional model of a dust layer, in *17th International Symposium on Shock Waves & Shock Tube, Bethlehem, PA*, edited by Yong W. Kim (1989).
38. T. Aki and F. Higashino, A numerical study on the implosion of polygonally interacting shocks and consecutive explosion in a box, in *17th International Symposium on Shock Waves & Shock Tube, Bethlehem, PA*, edited by Yong W. Kim (1989).